Materials Today Bio 37 (2026) 102884

Contents lists available at ScienceDirect

Materials Today Bio

journal homepage: www.journals.elsevier.com/materials-today-bio

Feasibility of combining JAK1 gene editing via CRISPR-CasRx with EGCG–lactoferrin nanoparticle therapy in a microneedle-based platform for atopic dermatitis

Huanqing Zhu [1], Haonan Yu [1], Mengxin Huang, Panjie Sun, Yuanfang Tang, Zhanyi Zhang, Puming He, Youying Tu, Bo Li [*]

Department of Tea Science, College of Agriculture and Biotechnology, Zhejiang University, 866 Yuhangtang Road, Hangzhou, 310058, China

ARTICLE INFO

Keywords:
Atopic dermatitis
JAK1
CRISPR-CasRx
EGCG
Lactoferrin
Microneedle

ABSTRACT

Atopic dermatitis (AD) is an inflammatory skin disease characterized by a complex pathogenesis. Current clinical treatments exhibit several limitations, including low efficacy and considerable side effects, prompting a growing interest in novel therapeutic strategies. In this study, we developed a microneedle-assisted dual-nano drug delivery strategy that targets both oxidative stress and Janus kinase 1 (JAK1) expression, aiming for enhanced therapy of AD. Self-assembling nanoparticles (NPs) incorporating epigallocatechin gallate (EGCG) and lactoferrin were developed to effectively modulate oxidative stress. Concurrently, CRISPR-CasRx technology was employed to silence JAK1, and nanoparticles were constructed by encapsulating CasRx and siRNA within poly (β-amino ester) (PBAE). Both types of NPs were successfully delivered to skin lesions in AD mice through microneedles, either individually or combined, resulting in significant alleviation of symptoms. Treatment reduced dermatitis severity scores and splenomegaly, decreased epidermal thickness and mast cell infiltration, and increased collagen fiber content. Additionally, levels of inflammatory cytokines (IL-1β, IL-4, IL-13) and oxidative DNA damage marker (8-OHdG) in dorsal skin tissues were lowered, accompanied by decreased serum levels of thymic stromal lymphopoietin (TSLP) and IgE. The therapy also suppressed JAK1 expression and activated the Nuclear factor erythroid 2-related factor 2 (Nrf2)/Heme oxygenase 1 (HO-1) antioxidant pathway, except for PBAE-plasmid NP-loaded microneedles, which did not significantly increase HO-1 expression. Notably, microneedles containing both NPs exhibited superior efficacy in reducing IL-1β and JAK1 levels and upregulating Nrf2 expression compared to formulations with only one NP type. This innovative combination strategy demonstrates promise as a novel therapeutic approach for AD.

1. Introduction

Atopic dermatitis (AD) is a chronic inflammatory dermatosis marked by recurrent skin lesions and allergic reactions. It is the 15th leading non-fatal disease and the most common skin disorder worldwide, affecting approximately 15–20% of children and about 10% of adults [1]. AD primarily arises from genetic, immune, and environmental factors, leading to impaired skin barrier function, dysregulation of inflammatory mediators, and the emergence of symptoms such as itching, swelling, and rash. Frequent itching and scratching in AD patients often result in sleep disturbances, significantly affecting their quality of life [2]. Current treatment approaches for AD involve repairing the skin barrier with emollients, using anti-inflammatory agents such as topical calcineurin inhibitors or corticosteroids, systemic immunosuppressants, phototherapy, and biological therapies. However, these treatment strategies often face challenges related to their effectiveness, side effects, patient adherence, and overall safety [3].

The Janus kinase (JAK)–signal transducer and activator of transcription (STAT) pathway is crucial in regulating the immunopathogenesis of AD. Typically, the JAK–STAT signaling pathway is activated when specific extracellular cytokines attach to their corresponding receptors. Once activated, JAKs phosphorylate tyrosine residues on these receptors as well as on other JAK proteins, creating sites for the recruitment and phosphorylation of crucial downstream signaling

* Corresponding author.
E-mail address: drlib@zju.edu.cn (B. Li).
[1] These authors equally contributed to this work.

https://doi.org/10.1016/j.mtbio.2026.102884
Received 24 May 2025; Received in revised form 17 October 2025; Accepted 30 January 2026
Available online 30 January 2026

components, particularly the STAT proteins. Upon phosphorylation, STAT proteins form dimers and migrate to the nucleus, where they attach to DNA and influence gene expression. Specifically, T helper type-2 (Th2) cytokines such as interleukin (IL)-31, IL-13, IL-5, IL-4, and thymic stromal lymphopoietin (TSLP) are significantly involved in the chronic inflammation and itching associated with AD, and their effects are mediated by the JAK–STAT signaling pathway. In addition, the JAK–STAT pathway is crucial for regulating the epidermal barrier and modulating peripheral nerves involved in itch sensation [4]. Currently approved JAK inhibitors for AD are predominantly designed to be highly selective for JAK1. Notable examples include upadacitinib and abrocitinib, which have been approved by U.S. Food and Drug Administration (FDA) and the European Medicines Agency (EMA) for AD management. The rationale for JAK1 selectivity stems from its central role in mediating the cytokine signaling pathways that drive key features of AD, namely inflammation and pruritus. By precisely disrupting these core pathogenic pathways, JAK1-selective inhibitors enable rapid relief from itching and improvement in skin lesions. Furthermore, as JAK2 is essential for hematopoietic signaling and JAK3 for lymphocyte development, selective JAK1 inhibition is anticipated to minimize off-target effects on vital physiological processes—such as hematopoiesis and immune homeostasis—thereby offering a potentially improved safety profile over broader-spectrum JAK inhibitors [5–7]. Nevertheless, these JAK inhibitors may carry various potential side effects, such as an elevated risk of herpes zoster, headaches, acne, increased blood creatinine phosphokinase levels, and nausea [8].

Gene therapy has attracted considerable global interest and has shown great potential in effectively treating a wide range of diseases. CRISPR-based gene-editing therapies hold considerable promise for the treatment of clinical diseases [9]. CRISPR/CasRx is an innovative RNA interference tool that harnesses a guide RNA (gRNA) along with the CasRx nuclease to selectively target and degrade specific RNA molecules. CasRx is a Cas13 nuclease derived from *Ruminococcus flavefaciens* strain XPD3002. Comprising approximately 930 amino acids, it is smaller than many other CRISPR-associated proteins, which facilitates easier incorporation into delivery vectors. One of the standout features of the CasRx protein is its low neurotoxicity in mammalian systems, enhancing its suitability for therapeutic applications. Unlike Cas9, which needs a protospacer adjacent motif (PAM) for recognizing its target, CasRx can bind to and cleave RNA without this limitation, allowing for greater versatility in target selection. Furthermore, since CasRx targets RNA instead of DNA, it minimizes the risk of permanent genomic alterations, making it a safer alternative for gene therapies [10, 11]. Targeting JAK1 for gene editing to improve AD is of significant research interest, but currently, there are no studies related to this approach.

The dysregulation of JAK/STAT signaling alone does not fully account for the entire pathogenesis of AD. Researchers are increasingly investigating combination therapies that incorporate JAK inhibitors to improve therapeutic efficacy while minimizing the side effects typically associated with these agents [12]. Oxidative stress is a major contributing factor in the onset of AD. Elevated levels of reactive oxygen species (ROS) lead to oxidative damage to DNA, proteins, and membrane lipids, resulting in cell death and worsening AD symptoms. ROS also activate the Toll-like receptor 4/myeloid differentiation primary response 88/nuclear factor-κB (TLR4/MyD88/NF-κB) signaling cascade, promoting T-cell differentiation and macrophage polarization, further facilitating AD progression. The interplay between oxidative stress and mechanical factors, such as scratching, complicates treatment. Scratching can increase oxidative stress and inflammation, while oxidative stress can enhance cellular sensitivity to mechanical stimuli. Additionally, ROS generated from environmental factors like dust mites and bacterial infections can harm endothelial cells, exacerbating the condition. Targeting the reduction of oxidative stress to repair the epidermal barrier could be an effective treatment strategy for AD [13, 14].

Plant polyphenols are recognized for their antioxidant and anti-inflammatory actives. They have demonstrated effectiveness in preventing skin damage and offer therapeutic benefits for various skin disorders, including psoriasis, alopecia, dermatitis, atopic eczema, and skin cancer [15]. Epigallocatechin-3-gallate (EGCG), a predominant bioactive catechin in tea, has demonstrated efficacy in improving AD-like skin lesions by inhibiting macrophage migration inhibitory factor (MIF) and various T helper 1 cytokines, including IL-2, IFN-γ, TNF-α, and IL-12 [16]. However, its pharmaceutical and cosmetic applications are hindered by certain drawbacks, including poor stability, limited skin permeability, and susceptibility to oxidation [17]. Nanotechnology plays a key role in the delivery of genes and small molecules in biomedical applications. It enables targeted delivery, ensuring that therapeutic agents reach specific cells or tissues. Additionally, it provides enhanced stability and protection, safeguarding delicate genetic material or compounds from degradation. Nanotechnology also facilitates controlled release, allowing for sustained and precise delivery of drugs and genes, which enhances delivery efficiency while reducing side effects [18]. Nanoparticle formulations demonstrate significant benefits in encapsulating EGCG for the management of several chronic diseases. A range of nanocarriers has been developed for the effective delivery of EGCG, including protein-based, carbohydrate-based, lipid-based, polymer-based, and metal-based nanoparticles [17].

Lactoferrin (LF) is a glycoprotein that binds iron and is present in the whey of mammalian milk. It is composed of roughly 700 amino acids and has a molecular weight of about 80 kDa [19]. LF not only possesses antibacterial, antiviral, immune-regulating, and iron-absorption-enhancing functions, but it can also serve as a nanocarrier for active ingredients. For instance, a novel nose-to-brain delivery system utilizing curcumin-LF nanoparticles has been developed, demonstrating significant neuroprotective effects both *in vitro* and *in vivo* [20]. Complexes of LF with hyaluronic acid have shown enhanced stability under heat, improved foaming and emulsifying properties, as well as increased antioxidant capacity and iron-binding strength [21].

Microneedle transdermal delivery offers a method of penetrating the epidermis to access the dermis while remaining within the non-innervated layers of the skin. In contrast to traditional injections, this technique bypasses the gastrointestinal tract and avoids first-pass metabolism in the liver. Consequently, it mitigates losses and potential side effects linked to first-pass metabolism. Additionally, microneedles are more convenient and virtually painless, leading to better patient compliance and improved treatment outcomes [22]. Therefore, combining in situ gene therapy for skin conditions with physical methods may optimize the effectiveness of *in vivo* gene therapy [23].

In this study, we aimed to treat AD by regulating oxidative stress in conjunction with silencing JAK1. On one hand, we prepared nanoparticles by self-assembling EGCG with LF. On the other hand, we designed a plasmid targeting JAK1 through CasRx-mediated gene editing and combined it with cationic poly (β-amino ester) (PBAE) to produce nanoparticles (NPs). Using microneedles, we delivered the dual nanoparticles transdermally, either separately or jointly, and the results suggested a significant improvement in AD symptoms in mice. The underlying molecular mechanisms involve the reduction of inflammation and oxidative stress, as well as the regulation of the JAK1 and Nuclear factor erythroid 2-related factor 2 (Nrf2)/Heme oxygenase 1 (HO-1) pathways (Scheme 1). This strategy shows promising potential for improving AD.

2. Materials and methods

2.1. Materials and reagents

EGCG (purity ≥ 98%) was acquired from Yuanye Biotechnology Co., Ltd. (Shanghai, China). Bovine LF (purity 95%) and hyaluronic acid (HA) were bought from Aladdin Biochemical Technology Co., Ltd. (Shanghai, China). Mouse embryonic fibroblast NIH/3T3 cells and

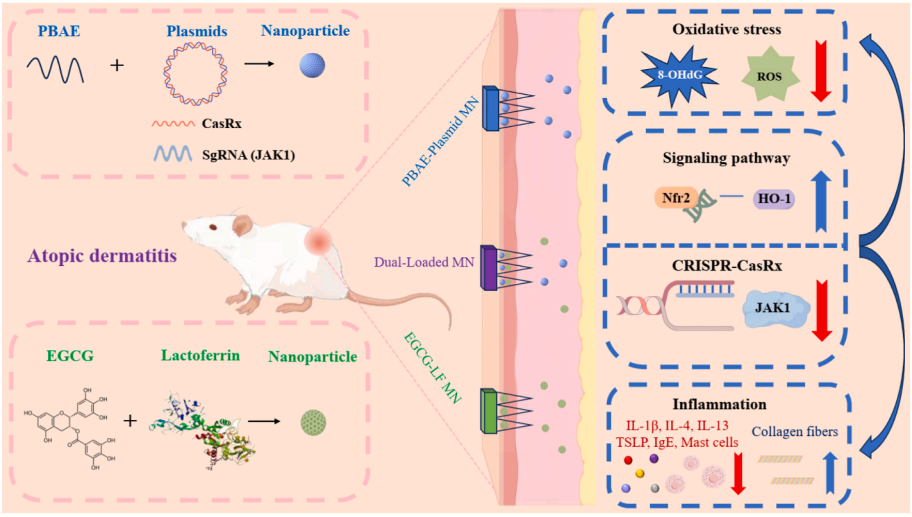

Scheme 1. Schematic illustration of microneedle delivery of JAK1-editing plasmids (CasRx) and EGCG-lactoferrin nanoparticles for the treatment of atopic dermatitis.

mouse dendritic DC2.4 cells were obtained from the American Type Culture Collection (ATCC). Human immortalized epidermal HaCaT cells were acquired from the China Center for Type Culture Collection (CCTCC). Lipo8000 ™ transfection reagents were supplied by Beyotime Biotechnology Co., Ltd (Shanghai, China). Acrylate, dinitrochlorobenzene (DNCB), cell culture media (DMEM and RPMI 1640) and fetal calf serum were bought from Sigma-Aldrich (St. Louis, MO, USA). Anhydrous dimethylformamide (DMF), 2,2'-(ethylenedioxy) bis (ethylamine), 3-methylaminopropylamine, tetrahydrofuran (THF), and dimethyl sulfoxide (DMSO) were purchased from Energy Chemical Co., Ltd (Shanghai, China). N-(2-aminoethyl) morpholine was purchased from TCI Development Co., Ltd. (Shanghai, China). The glyceraldehyde-3-phosphate dehydrogenase (GAPDH) antibody was obtained from Sanying Biotechnology Co., Ltd (Wuhan, China). Antibodies for JAK1, STAT3, p-STAT3, Nrf2, and HO-1 were purchased from Cell Signaling Technology, Inc. (Danvers, MA, USA). The microneedle mold was acquired from Chipu Medical Technology Co., Ltd (Xiamen, China). DiYO™-1 was sourced from AAT Bioquest (USA). Phycoerythrin (PE, 98% purity) was obtain from Jizhi Biochemical Technology Co., Ltd (Shanghai, China). The Masson's trichrome, toluidine blue, hematoxylin and eosin (H&E), mouse IL-1β ELISA kit, mouse IL-4 ELISA kit, and BCA protein quantitative detection kit were purchased from Sevier Biotechnology Co., Ltd. (Wuhan, China). The mouse IgE ELISA Kit and mouse TSLP ELISA Kit were sourced from Yuanju Biotechnology Center (Shanghai, China). The 8-OHdG ELISA Kit was purchased from Youersheng Technology Co., Ltd (Wuhan, China), and the mouse IL-13 uncoated ELISA kit was purchased from Lianke Biotechnology Co., Ltd (Hangzhou, China).

2.2. Preparation of EGCG-LF NPs and PBAE-plasmid NPs

To prepare EGCG-LF NPs, EGCG and LF were dissolved in phosphate-buffered saline (PBS) to create EGCG solutions ranging from 0.16 to 120 μM, alongside a 4 μM LF solution. The two solutions were combined in equal volumes to achieve various EGCG/LF molar ratios and allowed to self-assemble at room temperature for 30 min.

The plasmids pBS-CAG-CasRx-P2A-GFP-pA and pMD-20-Casrx-U6-gRNA backbone A+ were utilized for RNA editing. The sgRNA targeting mouse JAK1 was designed using the online tool available at https://cas13design.nygenome.org/ [24]. This sgRNA was then cloned into the pMD-20-Casrx-U6-gRNA backbone A+ vector using BpiI digestion. The primers for sgRNA preparation are detailed in Table S1. PBAE was synthesized and identified following the procedure outlined by Yan et al. [25]. Briefly, the synthesis ratio of linear poly (β-amino ester) (PBAE) was established at an acrylate-to-main chain amine ratio of 1:0.95. The components included acrylate, N-(2-aminoethyl) morpholine, and 3-methylaminopropylamine in a proportion of 1:0.5:0.2, dissolved in anhydrous dimethylformamide at a concentration of 150 mg/mL. The reaction mixture was stirred for 4 h at 40 °C, followed by a heating period of 48 h at 90 °C. Afterward, the mixture was cooled down to 30 °C, and excess 2,2'-(ethylenedioxy) bis(ethylamine) (1.5 molar equivalents) was added. To purify the polymer, the mixture was dropped into a cold anhydrous ether solution containing glacial acetic acid. Centrifugation at 1250 *g* for 2 min was performed to pellet the polymer, which was then washed with diethyl ether and dried under vacuum for 48 h. The resulting polymer was stored at −20 °C and could be dissolved using DMSO. The chemical structure of synthesized PBAE was verified using hydrogen nuclear magnetic resonance (NMR) spectroscopy. The PBAE was dissolved in a sodium acetate buffer (pH 5.0, 25 mM) at varying concentrations and subsequently added to a plasmid solution (100 ng) to prepare PBAE-plasmid NPs with different mass ratios. The mixture was pipetted and thoroughly mixed, then allowed to remain at room temperature for 30 min.

2.3. Characterization of nanoparticles

The average particle size, ζ-potential, and polydispersity index (PDI) of the NPs were assessed using Dynamic Light Scattering (DLS) with a Zetasizer Pro (Malvern Instruments, UK). The UV–visible absorption spectrum of EGCG-LF nanoparticles was recorded from 200 to 500 nm by a UV–visible spectrophotometer (Shimadzu, UV-2700, Japan). The fluorescence emission spectrum of EGCG-LF nanoparticles was obtained using a fluorescence spectrometer (FP-8500, JASCO, Japan), with an excitation wavelength of 280 nm, both excitation and emission slit widths set to 5 nm. The morphology of the prepared nanoparticles was examined using a transmission electron microscope (TEM, HT7700, Hitachi, Japan).

2.4. Encapsulation efficiency, loading capacity, and release rate of EGCG from EGCG-LF NPs

The EGCG-LF NPs were prepared using molar ratios of EGCG to LF of 1:1, 1:5, 1:10, 1:20, 1:25, and 1:30, as described above. To assess the EGCG release rate, the samples were incubated at 37 °C, and measurements were taken at 0, 1, 2, 4, 6, 8, 10, 12, and 24 h. The mixture was centrifuged at 10,000 g for 20 min at 4 °C, and the supernatant was

collected. The free EGCG content in the supernatant was then analyzed using high-performance liquid chromatography (HPLC, Agilent 1260 Infinity II, USA) equipped with an Intertail ODS-SP C18 column (5 μm, 250 × 4.6 mm, Shimadzu). Mobile phase A was comprised of acetonitrile, acetic acid, and water in a proportion of 3:0.5:96.5, whereas mobile phase B consisted of acetonitrile, acetic acid, and water in a ratio of 30:0.5:69.5. Gradient elution was performed over 0–35 min, gradually increasing the proportion of phase B from 30% to 80%. The temperature of the column was maintained at 25 °C, with a total flow rate set to 1 mL/min and a single injection volume of 10 μL. The detection wavelength was adjusted to 280 nm.

Encapsulation efficiency (EE), loading capacity (LC) and release rate of EGCG were determined using the respective formulas (1), (2), and (3).

$$EE = \frac{\text{Total mass of EGCG-Mass of free EGCG}}{\text{Total mass of EGCG}} \times 100\% \quad (1)$$

$$LC = \frac{\text{Total mass of EGCG-Mass of free EGCG}}{\text{Total mass of EGCG-LF NPs}} \times 100\% \quad (2)$$

$$\text{Release rate} = \frac{\text{Mass of free EGCG}}{\text{Total mass of EGCG in NPs}} \times 100\% \quad (3)$$

2.5. Molecular docking

The ligand EGCG was sourced from PubChem (https://pubchem.ncbi.nlm.nih.gov/), while the X-ray crystal structure of lactoferrin, with a resolution of 2.00 Å, was obtained from the RCSB Protein Data Bank (https://www.rcsb.org/structure/4U9C). Docking calculations were performed using AutoDock 4.2.6. A grid box was defined to encompass the active site of both EGCG and lactoferrin, with coordinates x = −9.632, y = −20.61, and z = −19.187. The number of Genetic Algorithm runs was set to ten, with all other parameters maintained at their default values. The best ligand-receptor complex for the docking simulation was chosen based on the minimal binding energy.

2.6. Total antioxidant capacity (T-AOC) assay

The total antioxidant capacity of the EGCG-LF NPs was assessed using the T-AOC Assay Kit (S0119, Beyotime, China). Following operational guidance, the 2,2′-azino-bis (3-ethylbenzthiazoline-6-sulfonic acid) (ABTS) working solution was prepared by diluting the ABTS stock solution with PBS. In a 96-well plate, 200 μL of the ABTS working solution was dispensed into each detection well, followed by the addition of 10 μL of the sample to the sample detection well and 10 μL of PBS to the blank control well. After incubating at room temperature for 6 min, the mixture's absorbance was recorded at 734 nm using a multimode microplate reader (BioTek Synergy H1, Agilent, America). The ABTS free radical scavenging activity was calculated using the following equation:

$$\text{ABTS free radical scavenging activity} = \left(1 - \frac{\text{A sample}}{\text{A control}}\right) \times 100\% \quad (4)$$

2.7. Cell viability assay

HaCaT, NIH/3T3, and DC2.4 cells were inoculated into a 96-well plate with DMEM supplemented with 10% FBS and 1% penicillin/streptomycin. The plates were incubated overnight at 37 °C with 5% CO_2. Following this, the cells were treated with EGCG, EGCG-LF NPs, or PBAE-plasmid NPs for 24 h. The medium was then removed, and the cells were rinsed twice with fresh medium. Following this, the cells were incubated with new medium containing 10% CCK-8 solution (UElandy, Suzhou, China) for 30 min. The absorbance was recorded at 450 nm using a microplate reader (Thermo, MK3, MA, USA).

To investigate whether the samples can improve H_2O_2 and DNCB-induced cell damage, HaCaT cells underwent pre-treatment with H_2O_2 (1 mM) for 4 h or with DNCB (60 μM) for 2 h. After discarding the culture medium, the cells were incubated with fresh medium containing either EGCG or EGCG-LF NPs for 24 h. Cell viability was evaluated using the CCK-8 assay.

2.8. Determination of intracellular reactive oxygen species (ROS)

To assess the ROS-scavenging capacity, HaCaT cells were cultured in 24-well plates at a density of 50,000 cells per well for 24 h. Following this, the cells were treated with culture medium containing 1 mM H_2O_2 for 4 h to induce oxidative stress. Afterward, the medium was substituted with fresh culture medium containing either EGCG or EGCG-LF NPs and incubated for 30 min. Subsequently, the medium was exchanged for a solution of 5 μM DCFH-DA (S0033S, Beyotime, China), and the cells were incubated for an additional 10 min. The green fluorescence signals in the cells were then detected using a fluorescence microscope (IX71, Olympus, Japan), and fluorescence intensity was determined using ImageJ software.

2.9. Assay of superoxide dismutase (SOD), catalase (CAT), and malondialdehyde (MDA)

HaCaT cells were seeded in 96-well plates at a density of 8000 cells per well and cultured for 24 h. The cells were then exposed to 1 mM H_2O_2 for 4 h to induce oxidative stress. After this treatment, the medium was replaced with fresh medium containing either free EGCG or EGCG-LF NPs for a further 24 h. Subsequently, the activities of SOD and CAT, as well as the MDA level, were assessed using the Superoxide Dismutase Colorimetric Activity Kit (EIASODC), the Hydrogen Peroxide/Peroxidase Detection Kit (A22188), and the Malondialdehyde Colorimetric Assay Kit (EEA015) (Thermo Fisher Scientific, Waltham, MA, USA), respectively, following the manufacturers' protocols.

2.10. Determination of intracellular EGCG content

HaCaT cells were seeded in 6-well plates at a density of 1×10^6 cells per well and allowed to adhere for 24 h. Following three washes with PBS, the cells were incubated with either free EGCG or EGCG-LF NPs in PBS for 4 h. After treatment, the cells were washed three times with PBS and lysed using an ultrasonic homogenizer. The resulting lysates were filtered through 40 μm filters, collected, and adjusted to a final volume of 500 μL. These samples were then passed through 0.45 μm filters, and the EGCG content was quantified by HPLC as described in Section 2.4.

2.11. Gel retardation assay

For the gel electrophoresis experiments, the plasmid was fixed at a concentration of 100 ng, with varying amounts of PBAE added to achieve the different PBAE-plasmid ratios. The prepared complexes were then loaded into a pre-made 1% agarose gel and subjected to electrophoresis at 160 V for 25 min. After electrophoresis, the gel was visualized using a Bio-Rad imaging system to capture images for observation.

2.12. Gene transfection

To assess the effects of gene editing *in vitro*, NIH/3T3 and DC2.4 cells were plated in six-well plates one day prior to transfection, allowing the cell density to reach 70–80% during the culture period. Before transfection, the culture medium was changed to serum-free RPMI 1640 medium. The cells were then incubated with PBAE-plasmid nanoparticles (NPs) for 6 h, after which the medium was replaced with complete DMEM culture medium. Following an additional 48-h incubation, the GFP fluorescence intensity in the cells was observed and photographed using a fluorescence microscope.

For the *in vivo* studies, PBAE-plasmid NPs were injected into the back skin of mice via subcutaneous injection. After 24 h, the mice were

euthanized, and the skin at the injection site was harvested for total RNA and protein extraction. Real-time quantitative PCR was conducted to evaluate the knockout efficiency of the target gene, while Western blotting was employed to quantitatively assess the expression efficiency of the target protein.

2.13. Fabrication and characterizations of MN patches

The dimensions of the MN patch were 12.5 mm by 12.5 mm, featuring a 15-by-15 array. Each needle cavity had a base side length of 320 μm, a height of 800 μm, and a tip distance of 650 μm. An 8% HA solution containing EGCG-LF NPs and PBAE-plasmid NPs was poured into the microneedle mold. The excess solution was removed, and the mold was dried under vacuum for 15 min to form a hydrogel. Subsequently, 500 μL of HA solution was deposited on the microneedles and stored in a dry location at room temperature overnight. After complete drying, the MN patch was carefully separated from the mold. Macroscopic observations of the microneedles were conducted using a handheld microscope (UM039, BOSHILE, China), while the morphology and dissolution of the microneedles after insertion into the skin were examined using a scanning electron microscope (SEM, SU8010, HITACHI, Japan). Fluorescence images of the microneedles loaded with EGCG-LF NPs labeled with PE and PBAE-plasmid NPs labeled with DiYO™-1 were captured using a confocal microscope (FV3000, Olympus, Japan). To measure the mechanical strength of the MN patches, they were placed tip-upward and subjected to pressure using a universal testing machine (model 5944, INSTRON, USA) at a speed of 10 μm/s. During the process, both the displacement and the pressure applied to the tips were recorded.

2.14. Measurement of drug release from MN patches

The release of EGCG and plasmids from MN patches was assessed both *in vitro* and *in vivo*. For the *in vitro* study, the tip of the microneedle patch was soaked in a PBS solution at 37 °C. At set time intervals, PBS was collected and replaced with an equal volume of fresh PBS. The collected solution was then filtered using a 0.22 μm polyvinylidene fluoride filter, and the EGCG content was quantified using the HPLC method detailed in Section 2.4. The PBAE-plasmid NPs were labeled with DiYO™-1, and the fluorescence intensity in the collected PBS solution was measured with a multimode microplate reader (BioTek Synergy H1, Agilent, USA). To visualize drug release *in vivo*, skin sections were harvested 24 h following MN patch application. The EGCG-LF NPs, labeled with PE, and the PBAE/DNA NPs, labeled with DiYO™-1, were visualized using a confocal microscope (FV3000, Olympus, Japan).

2.15. DNCB-induced AD mouse model and treatment

Male BALB/c mice, aged 6–8 weeks, were acquired from Hangzhou Medical College and housed under controlled conditions at a temperature of (23 ± 3 °C) with a relative humidity between 40 and 60%. All experiments involving animals were conducted according to the ethical policies and procedures approved by the Experimental Animals Ethics Committee of Zhejiang University (Approval no. ZJU20250099). Following one week of acclimatization, the mice were shaved on their backs and allowed to adapt for an additional 2 days. The animals were then randomly assigned to five groups: control, model, MN patch loaded with EGCG-LF NPs, MN patch loaded with PBAE-plasmid NPs, and MN patch dual-loaded with EGCG-LF NPs and PBAE-plasmid NPs. AD was induced by applying 200 μL of a 1% (w/v) DNCB solution in an acetone/olive oil mixture (3:1) to a restricted area of the back skin every two days for the first week. From the second week onward, 200 μL of a 0.5% (w/v) DNCB solution in the same acetone/olive oil mixture was applied twice a week for an additional four weeks. The MN patches were applied topically to the mice biweekly for five weeks. Each patch was firmly pressed against the skin for 2 min to facilitate penetration through the stratum corneum and epidermis. Subsequently, gentle pressure was applied for an additional 30 s to enhance fluid absorption into the patch. To ensure sustained drug release, the MN patches were further secured in place using medical tape. Mouse body weights were recorded weekly, and skin severity scores were assessed twice weekly after the first week. AD severity scores were calculated as the sum of four measured symptoms: edema, desquamation/dryness, erythema/hemorrhage, and ulceration/exfoliation. Each symptom was rated on a scale: 0 (no symptoms), 1 (mild), 2 (moderate), or 3 (severe). After five weeks of treatment, the mice were sacrificed to collect skin tissue, spleen, and blood samples. The spleen weight was recorded, and the spleen index was calculated using the equation: Spleen index = spleen weight (mg)/body weight (g).

2.16. Quantitative real-time PCR analysis

Total RNA was extracted from both cellular and animal skin tissues using the Trizol method. Subsequently, reverse transcription to cDNA was conducted with the HiScript III 1st Strand cDNA Synthesis Kit (Novozymes, Nanjing, China). qRT-PCR was conducted on a StepOnePlusTM Real-Time PCR System (Applied Biosystems, Foster City, CA, USA) with TB Green® Premix Ex TaqTM II (Takara, Beijing, China). Relative mRNA expression levels were analyzed using the comparative Ct method (ΔΔCt) and normalized against the endogenous β-actin. The primer sequences utilized in this study are detailed in Table S2.

2.17. Western blot

Total protein extraction was performed using RIPA lysis buffer. Protein concentrations were determined using a BCA Protein Assay Kit from Beyotime Biotech Inc (Shanghai, China). The samples were separated by 12% SDS-PAGE and subsequently transferred to polyvinylidene fluoride (PVDF) membranes using a Mini-Protean 3 System (BioRad). The membranes were treated with a blocking solution consisting of 5% bovine serum albumin (BSA) in Tris-buffered saline with Tween (TBST) at room temperature for 1 h. This was followed by a series of incubations with primary and secondary antibodies. The bands were visualized using the BeyoECL Plus kit (Beyotime Biotech Inc, Shanghai, China) and analyzed using ImageJ software (NIH, Bethesda, MD, USA).

2.18. Enzyme-linked immunosorbent assay (ELISA)

Tissue samples were mixed with 0.9% physiological saline at a weight-to-volume ratio of 1:9 (mg: μL) to prepare a 10% homogenate under ice water bath conditions. The solution was subsequently spun at 2500 rpm for 10 min, after which the supernatant was obtained for further analysis. Blood samples were placed in an ice bath for 1 h to allow separation of serum and blood. Subsequently, the centrifuge tubes were centrifuged at 2500 rpm for 30 min at 4 °C. The processed tissue and serum samples were analyzed according to the instructions provided with the ELISA kit.

2.19. Histological analysis

Mouse back skin was harvested for histological analysis. The tissues were fixed in 4% paraformaldehyde and dehydrated in alcohol. Tissues embedded in paraffin were sectioned into 20 μm thick slices and stained using hematoxylin and eosin (H&E), toluidine blue (TB), and Masson's trichrome to assess epidermal thickness, mast cell count, and collagen deposition recovery.

2.20. Immunofluorescence (IF) assay

The tissue sections were treated with normal goat serum to block non-specific interactions and were then incubated overnight with primary antibodies specific to Nrf2 and HO-1. Following this, the samples were stained with a secondary antibody and 4',6-diamidino-2-

phenylindole (DAPI). Fluorescence images were captured using a confocal microscope (Olympus, FV3000, Tokyo, Japan), and the fluorescence intensity was evaluated using the ImageJ 1.54p software (NIH, Bethesda, MD, USA).

2.21. Statistical analysis

The data are expressed as means ± standard deviations (SD), and all analyses were conducted using SPSS 26.0 software (SPSS Inc., Chicago, IL, USA). A one-way analysis of variance (ANOVA) followed by the Duncan test was used to assess the significance of differences among the groups. A p-value of less than 0.05 was considered statistically significant.

3. Results and discussion

3.1. Characterization of the EGCG-LF NPs

In this research, we first explored the interaction between EGCG and LF, as well as the characteristics of the resulting complex. As shown in Fig. 1a, the maximum fluorescence emission peak of LF is at 332 nm. With the rising concentration of EGCG, the intrinsic fluorescence of LF progressively decreased, accompanied by a red shift in the absorption peak. Tryptophan residues serve as the primary luminescent groups in LF. The variation in fluorescence intensity indicated the fluorescence quenching that occurred when LF complexed with EGCG. Additionally, the shift in λ_{max} provided insights into the oxidation state of the tryptophan residues, as well as alterations in the protein's tertiary structure and its microenvironment [21]. Fig. 1b illustrates that both EGCG and LF exhibit maximum ultraviolet (UV) absorption wavelengths in the 270–280 nm range. The EGCG peak is attributed to UV light absorption by the benzene ring structures in the molecule [26]. LF's absorption peak is primarily due to the presence of amino acid residues including phenylalanine, tryptophan, and tyrosine, which show strong UV absorption near 280 nm [27]. The increase in UV absorption observed after mixing suggests an interaction between EGCG and LF, without significantly affecting the functional groups responsible for UV absorption in either molecule. Fig. S1 demonstrates the molecular docking of EGCG with LF. The analysis revealed that EGCG interacted with the amino acid residues THR-430 and GLY-652, establishing two hydrogen bonds. The binding energy of this interaction has been calculated to be −4.93 kcal/mol, indicating an affinity between EGCG and LF. Phenols interact with proteins mainly through non-covalent forces, such as electrostatic attractions, hydrogen bonds, and hydrophobic interactions. These interactions can result in the creation of new complexes that may exhibit improved functional characteristics and biological activities [28].

To optimize the EGCG to LF ratio, we evaluated the particle size and polydispersity index (PDI) at various molar ratios (0, 1/25, 1/10, 1/5, 1, 20, 25, 30). Dynamic light scattering (DLS) analysis indicated that increasing the molar ratio of EGCG to LF initially decreased the particle size, followed by an increase, while the PDI showed an initial increase followed by a decrease. At a molar ratio of 25, the assembled EGCG-LF NPs demonstrated an approximate particle size of 35.5 nm and a PDI of 0.28, suggesting a relatively uniform size distribution (Fig. 1c). Transmission electron microscopy (TEM) images illustrated that the EGCG-LF complex had a monodisperse spherical structure, with a size consistent with the DLS analysis data (Fig. 1d). These observations emphasized the critical role of the interaction dynamics between EGCG and LF. The homogeneity of the particle population improved as the optimal ratio is

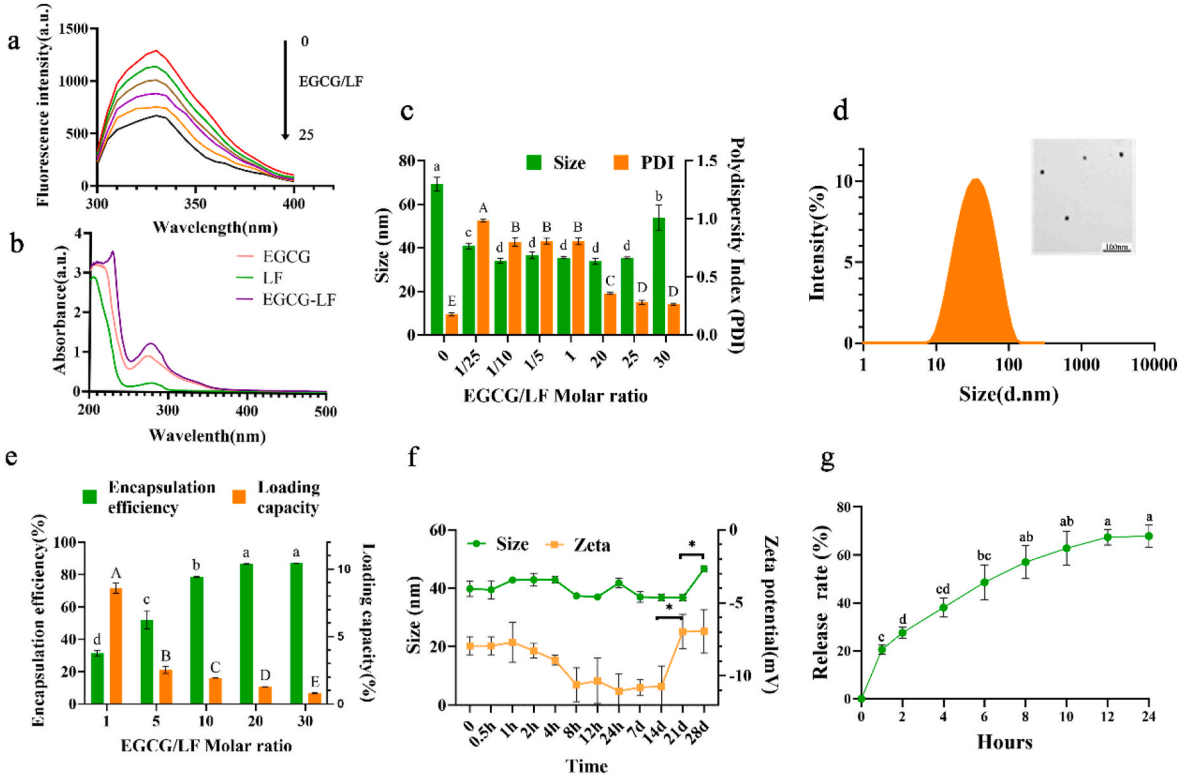

Fig. 1. Characterization of EGCG-LF NPs. (**a**) Fluorescence spectra of EGCG-LF NPs at various EGCG/LF molar ratios (0, 1, 5, 10, 20, 25). (**b**) Ultraviolet absorbance spectra of EGCG, LF, and EGCG-LF NPs with an EGCG/LF molar ratio of 25. (**c**) Particle size and polydispersity index (PDI) of EGCG-LF NPs at different EGCG/LF molar ratios. (**d**) Size distribution analyzed by dynamic light scattering (DLS) and the transmission electron microscopy (TEM) image of EGCG-LF NPs at an EGCG/LF molar ratio of 25. (**e**) Encapsulation efficiency and loading capacity of EGCG at varying EGCG/LF ratios. (**f**) Particle size and zeta potential of EGCG-LF NPs measured over time. (**g**) Release profile of EGCG from EGCG-LF NPs in PBS at 37 °C over 24 h. Data are presented as mean ± SD (n = 3). The LF concentration was fixed at 4 μM. Bars sharing the same letter are not significantly different, whereas those with different letters are statistically significant ($p < 0.05$). *$p < 0.05$.

approached. As the ratio progressed, the availability of EGCG might result in increased aggregation effects, potentially due to hydrophobic interactions that facilitate the self-assembly process [29].

Increasing the molar ratio of EGCG to LF led to an increase in encapsulation efficiency (EE) from (31.39 ± 1.29) % to (87.06 ± 0.99) %, while the loading capacity (LC) decreased from (8.60 ± 0.32) % to (0.79 ± 0.04) % (Fig. 1e). This was primarily due to the increased concentration of EGCG, which led to a greater participation of LF proteins in self-assembly, thereby having a more significant impact on the quality of the nanoparticles. Stability testing showed that the average particle size of the EGCG-LF NPs (EGCG to LF molar ratio, 25:1) remained stable around 40 nm until day 21, increasing slightly to 46.7 nm on day 28, with the zeta potential maintained between approximately −7 and −11 mV throughout this period (Fig. 1f). The release of EGCG from EGCG-LF NPs (EGCG to LF molar ratio, 25:1) in PBS gradually rose to approximately 68% over 12 h, then plateaued (Fig. 1g). These data indicated that the EGCG-LF NPs exhibited good stability and suggested that this approach offers an effective strategy for controlling the release of EGCG over the observed period. Numerous studies have shown that LF-based nanoparticles enhance the chemical stability of small bioactive molecules under varying pH levels, high ionic strengths, and temperature changes. This improvement will facilitate the application of these active substances in a broader range of environments [30,31].

3.2. *Preservation of antioxidant activity and cytoprotective effects of EGCG-LF NPs*

The total antioxidant capacity of the EGCG-LF NPs was assessed using the ABTS assay. As shown in Fig. 2a, both EGCG and EGCG-LF NPs initially exhibited ABTS free radical scavenging rates exceeding 90%. Over a 28-day period, the ABTS free radical scavenging activities of both EGCG and EGCG-LF NPs decreased; however, EGCG-LF NPs consistently demonstrated higher activity than EGCG alone, with clearance rates around 10% greater. A comparable conclusion was obtained by Li et al. (2010), who found that nanoparticles formed from β-lactoglobulin and EGCG through a self-assembly method were able to maintain the

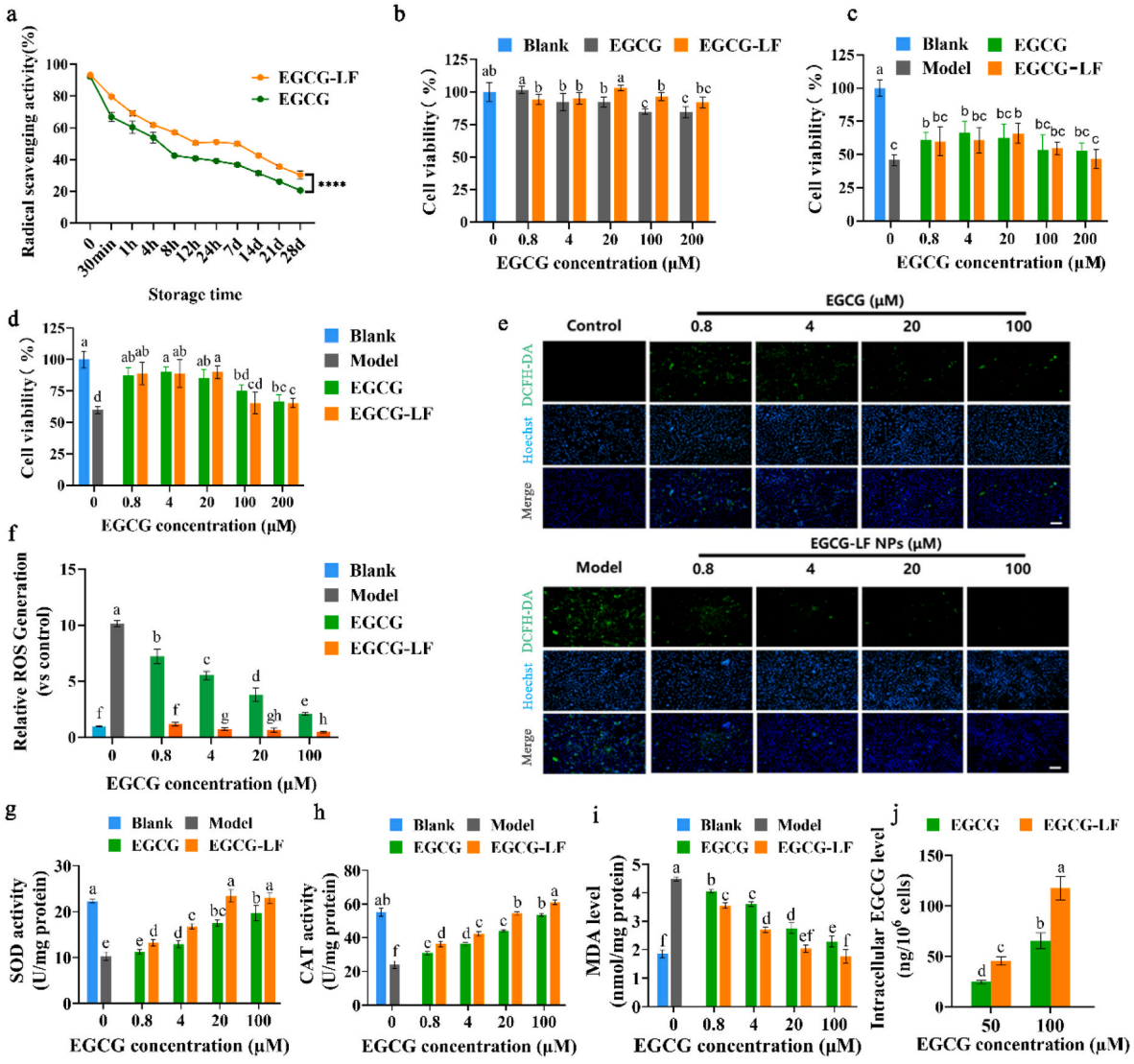

Fig. 2. Antioxidant activity and cytoprotective effects of EGCG-LF NPs compared to EGCG. (**a**) ABTS radical scavenging activity over a period of 28 days. (**b**) Effect of EGCG and EGCG-LF NPs on HaCaT cell viability. (**c**) Cytoprotective effects of EGCG and EGCG-LF NPs on HaCaT cells treated with DNCB. (**d**) Cytoprotective effects of EGCG and EGCG-LF NPs on HaCaT cells treated with H_2O_2. (**e**) Intracellular ROS scavenging activity of EGCG and EGCG-LF NPs in H_2O_2-treated HaCaT cells. Green and blue fluorescence represent ROS proteins and nuclear DNA (nDNA), respectively. Scale bar = 100 μm. (**f**) Quantitative analysis of (e). (g–i) Effects of EGCG and EGCG-LF NPs on SOD and CAT activities and MDA levels in H_2O_2-treated HaCaT cells. (j) Intracellular EGCG levels in HaCaT cells after 4-h incubation with EGCG or EGCG-LF NPs. Data are presented as mean ± SD (n = 3). Bars sharing the same letter are not significantly different, whereas those with different letters are statistically significant ($p < 0.05$). ****$p < 0.0001$.

antioxidant efficacy of EGCG. This preservation is primarily attributed to the protective nature of the nanoparticle structure, which enhances the stability of EGCG [32].

Keratinocytes, the main cell type in the epidermis, are essential in establishing the skin barrier. Under stimulation by various allergens, keratinocytes release pro-inflammatory mediators [2]. The human keratinocyte cell line HaCaT is widely used in dermatological studies, particularly for modeling AD, as these cells can mimic AD symptoms in response to oxidative stress [33]. In this work, HaCaT cell viability was measured using the CCK-8 assay to evaluate the cytotoxic effects of EGCG-LF NPs. As shown in Fig. 2b, cell viability decreased at higher concentrations of EGCG treatment compared to the blank group ($p < 0.05$). Notably, EGCG-LF NPs exhibited lower cytotoxicity toward HaCaT cells than EGCG alone, particularly at EGCG concentrations ranging from 20 to 100 μM, where the differences were statistically significant ($p < 0.05$). High levels of EGCG uptake have been associated with cytotoxic effects on normal cells [34]. Nanotechnology can mitigate this damage to normal tissues by regulating the release of EGCG, reducing oxidative stress caused by its auto-oxidation, and enhancing targeting efficiency [35].

Modulating oxidative stress through ROS scavenging presents a promising strategy for regulating the immune environment in AD [36]. To investigate the protective effects of EGCG and EGCG-LF NPs on HaCaT cells stimulated with DNCB and H_2O_2, we first evaluated the impact of various DNCB (0, 10, 20, 40, 60, and 80 μM) and H_2O_2 (0, 100, 200, 400, 800, 1000, and 2000 μM) concentrations on cell growth. Based on this assessment, we selected 60 μM DNCB and 1000 μM H_2O_2 for further testing, as these concentrations significantly decreased cell viability to approximately 55–60% (Fig. S2). Both EGCG and EGCG-LF NPs effectively enhanced cell viability compared to the model groups, particularly within the lower concentration range of 0.8–20 μM (Fig. 2c and d). We then compared the ROS-scavenging capacity of EGCG and EGCG-LF NPs in HaCaT cells treated with 1000 μM H_2O_2. At equivalent EGCG concentrations, the EGCG-LF NPs demonstrated significantly superior scavenging capabilities compared to EGCG alone (Fig. 2e and f). EGCG-LF NPs demonstrated a superior capacity to preserve the activities of SOD and CAT ($p < 0.05$), and were more effective in lowering MDA levels ($p < 0.05$) in H_2O_2-exposed HaCaT cells compared to free EGCG (Fig. 2g–i). When HaCaT cells were treated with equivalent concentrations of free EGCG or EGCG-LF NPs (50 and 100 μM EGCG), HPLC analysis showed that the intracellular EGCG contents delivered via EGCG-LF NPs was approximately 1.8-fold higher than that achieved with free EGCG ($p < 0.05$), indicating enhanced cellular uptake efficiency of EGCG when encapsulated in LF NPs (Fig. 2j). Previous research indicated that curcumin, when encapsulated in LF nano-micelles, significantly mitigated oxidative stress damage induced by H_2O_2 in endothelial cells. This formulation enhanced cell viability and restored the mitochondrial membrane electrical potential [37]. The LF-quercetin nano gel demonstrated enhanced free radical scavenging activity and improved antioxidant enzyme activity (including SOD and CAT) compared to lactoferrin and quercetin alone [38]. The use of nanotechnology can enhance cellular uptake and enable localized delivery of antioxidants, presenting promising strategies for the development of advanced dermatological formulations designed to prevent and treat skin disorders related to oxidative stress [39].

3.3. Characterization and gene editing efficiency of PBAE-plasmid NPs

Inhibiting JAK1 expression could significantly impact the signaling pathways of various immune and epidermal cell cytokines involved in the pathogenesis of AD. While JAK1 inhibitors have demonstrated good efficacy in treating patients with AD, they also come with certain side effects [8,40]. CasRx-mediated knockdown has demonstrated greater efficiency and specificity compared to RNA interference (RNAi), making it a promising approach for modulating various endogenous transcripts [41]. In the present study, CRISPR/CasRx was employed to silence JAK1, and four sgRNA sequences specifically targeting JAK1 were designed. Then plasmids containing different sgRNA sequences were transfected into NIH/3T3 and DC2.4 cells using the commercial cell transfection reagent Lipo8000™. The results indicated that the sgRNA 2 sequence exhibited the highest knockdown efficiency in both cells (Fig. 3a–b), leading to its selection for subsequent experiments.

PBAE is a highly promising candidate for gene editing plasmid delivery due to its advantageous properties, such as biocompatibility, efficient encapsulation, and effective transfection capabilities [42]. To prepare PBAE-plasmid NPs, PBAE (Fig. S3) and plasmid were combined in various mass ratios to determine the optimal formulation. As depicted in Fig. 3c, when the mass ratio of PBAE to plasmid was below 20, the NPs exhibited a negative charge, accompanied by an average particle size exceeding 700 nm. In contrast, when the mass ratio ranged from 20 to 500, the nanoparticles displayed a positive charge, with an average particle size of approximately 500 nm. The gel electrophoresis analysis demonstrated that as the mass ratio of PBAE to the plasmid increased, DNA migration was progressively inhibited (Fig. 3d). This finding aligns with the Zeta potential analysis, which indicated that PBAE neutralized the negative charge on the DNA, causing the complex's charge to shift from negative to positive. DLS analysis demonstrated that the particle sizes of the samples varied between 100 nm and 1000 nm when the PBAE-plasmid ratio was 20/1 (w/w), with a mean size of about 500 nm. TEM imaging confirmed that the particles had a similar diameter to that indicated by the DLS data and revealed the presence of uniformly spherical structures (Fig. 3e).

The NIH/3T3 and DC2.4 cells were exposed to PBAE-plasmid NPs with varying mass ratios, while maintaining a constant plasmid mass of 100 ng. As illustrated in Fig. 3f–g, when the mass ratio of PBAE to plasmid was between 0 and 30, there was no significant impact on the viability of NIH/3T3 and DC2.4 cells. The PBAE-plasmid NPs at a mass ratio of 20:1 were transfected into NIH/3T3 cells, resulting in a significant increase in intracellular green fluorescence (Fig. 3h) and a marked reduction in JAK1 mRNA levels (Fig. 3i), indicating successful transfer of the plasmids into the cells. To further validate the gene transfection efficiency *in vivo*, the PBAE-plasmid NPs was subcutaneously injected into the back of mice. There was a remarkable downregulation of JAK1 protein in contrast to the control group, with quantitative analysis confirming the significant reduction in JAK1 protein expression (Fig. 3j). These results indicated that this PBAE-plasmid NPs could effectively enter cells both *in vitro* and *in vivo*, leading to a decrease in JAK1 expression. Compared to JAK1 inhibitors, this method may have greater specificity and reduced the risk of side effects caused by off-target binding [43].

3.4. Characterization and drug release of the MN patch

Microneedles are an emerging technology for the transdermal delivery of phytochemicals and biomacromolecules. They have been used in treating a variety of conditions, such as skin disorders, type 2 diabetes, arthritis, etc. [44]. In this study, we prepared a MN patch for delivering nanoparticles aimed at treating AD. Microscopic observation revealed that the microneedles of the blank MN patch were neatly arranged and exhibited a regular, straight quadrangular pyramid shape (Fig. 4a). With increasing concentrations of EGCG-LF NPs (0–40 mg/mL) in the hyaluronic acid hydrogel, the system transitioned from colorless and transparent to yellow, accompanied by an increase in viscosity (Fig. S4). Additionally, SEM images revealed the smooth, flat surface of the microneedles with sharp tips (Fig. 4b). Mechanical testing with a universal testing machine demonstrated that microneedles loaded with 20 mg/mL EGCG-LF NPs required the highest force for the same displacement, indicating optimal mechanical properties (Fig. 4c). A previous study has shown that the addition of collagen tripeptide can enhance the mechanical strength of HA-based microneedles [45]. LF may modify the mechanical properties of the microneedles by interacting with HA through both cross-linking and non-covalent binding

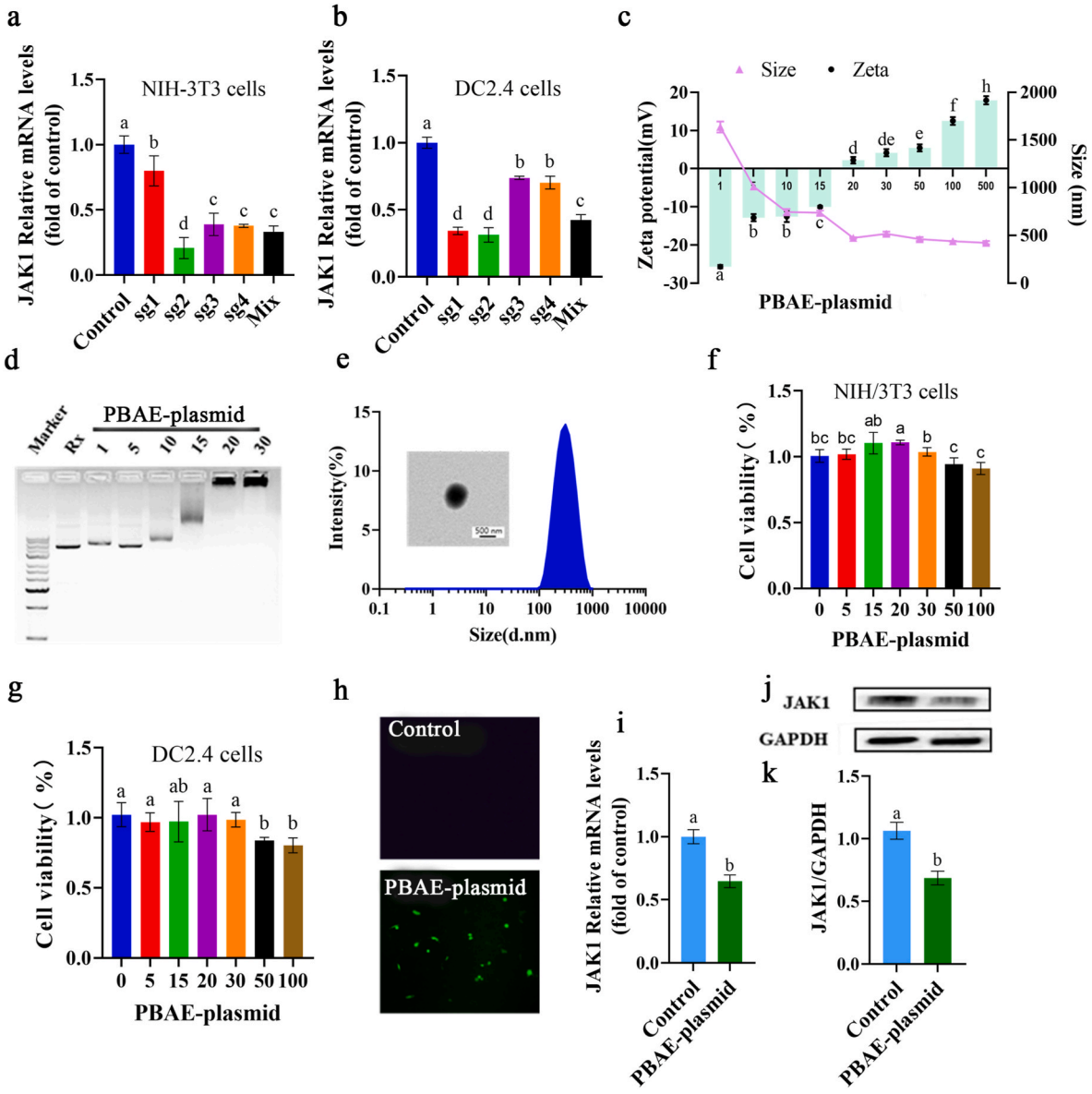

Fig. 3. Characterization and gene editing efficiency of PBAE-Plasmid NPs. (**a**) and (**b**) RNA silencing effects of different sgRNAs targeting JAK1 in NIH-3T3 and DC 2.4 cells. (**c**) Size and zeta potential of the PBAE-plasmid complex at various mass ratios. (**d**) Agarose gel electrophoresis of the PBAE/plasmid complex at different mass ratios. (**e**) Size distribution analyzed by dynamic light scattering (DLS) and transmission electron microscopy (TEM) images of PBAE-plasmid NPs at a mass ratio of 20:1. (**f**) and (**g**) Effects of the PBAE-plasmid complex at various mass ratios on NIH-3T3 and DC 2.4 cell viability. (**h**) Green fluorescence in NIH-3T3 cells transfected with PBAE-plasmid NPs. (**i**) JAK1 mRNA expression in NIH-3T3 cells transfected with PBAE-plasmid NPs. (**j**) JAK1 protein expression in mice transfected with PBAE-plasmid NPs. (**k**) Quantitative analysis of (j). Data are presented as mean ± SD (n = 3). Bars sharing the same letter are not significantly different, whereas those with different letters are statistically significant ($p < 0.05$).

[46].

To visualize the drug-loading effect of microneedles, PBAE-plasmid NPs and EGCG-LF NPs were stained with fluorescent dyes DiYO™-1 (green) and phycoerythrin (PE, red), respectively, and were examined using a confocal microscope. Fig. 4d shows even distribution of green and red fluorescence within the microneedles, confirming successful loading of both nanoparticles. Fig. 4e–f shows the *in vitro* release rates of PBAE-plasmid NPs and EGCG-LF NPs in microneedles both exceeded 60% at 24 h, and reached 82.6% and 89.8% at 72 h. Following the application of the MN patch on the dorsal skin of the mice, the SEM images show the microneedles partially dissolve within 60 s (Fig. 4g). Atopic dermatitis involves impaired barrier function of the epidermis and infiltration of multiple immune cells into the dermis. Therefore, treatment should take a dual approach, addressing both epidermal barrier restoration and dermal inflammation [47,48]. The typical thickness of mouse skin is approximately 10–25 μm for the epidermis and 200–400 μm for the dermis. Confocal microscopy of frozen skin sections, with a white scale bar (200 μm) in the lower-right corner of the bright-field image, demonstrated effective delivery of both loaded nanoparticles into the epidermis and dermis (Fig. 4h). These data confirmed that the developed MN patches possess promising characteristics for the efficient delivery of both nanoparticles.

Hyaluronic acid (HA) is commonly used to fabricate dissolvable microneedles based on the “poke and release” principle. Uncrosslinked HA molecules form a hydrogel with a loose molecular network. Upon administration, this polymer matrix dissolves, releasing the encapsulated agents [49]. Even when chemically crosslinked with agents such as 1,4-butanediol diglycidyl ether (BDDE) to covalently connect HA molecules (at concentrations of 7.0–14.0% w/v) and form a stable three-dimensional network, the pore sizes typically remain in the range

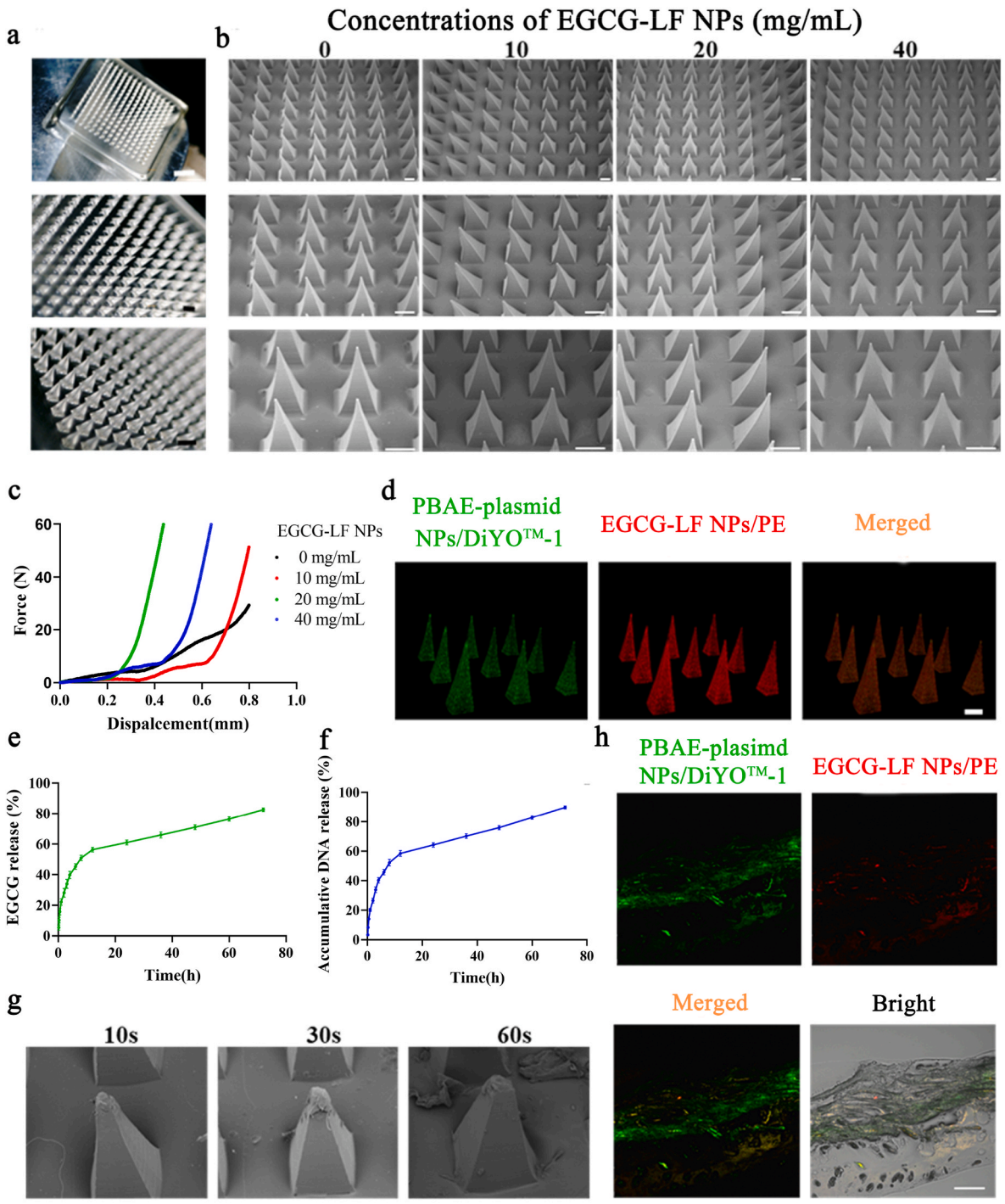

Fig. 4. Characterization and drug release of the MN Patch. (**a**) Microscope images of the blank MN patch. White scale bar = 2.5 mm; black scale bar = 650 μm. (**b**) SEM images of the MN patch loaded with different concentrations of EGCG-LF NPs. Scale bar = 200 μm. (**c**) Mechanical strength of MN patches loaded with various concentrations of EGCG-LF NPs. (**d**) Fluorescence images of the MN patch containing PBAE/plasmid NPs loaded with DiYO™-1 (green) and EGCG-LF NPs loaded with PE (red). Scale bar = 200 μm. (**e**) and (**f**) *In vitro* release of EGCG and plasmid from the MN patch. (**g**) SEM images of the MN patch at 10 s, 30 s, and 60 s after insertion into mouse skin. (**h**) Fluorescence images of mouse skin after insertion of the MN patch. Scale bar = 200 μm.

of several tens to several hundreds of micrometers [50]. This may explain why the substantial differences in particle size did not significantly affect their release from the microneedles. The physical and chemical properties of nanoparticles, such as size and surface charge, are critical factors influencing their cellular uptake. These characteristics determine which endocytic pathway is utilized and impact the overall efficiency of internalization. Typically, smaller NPs (10–200 nm) are taken up primarily through processes like clathrin-mediated endocytosis, caveolin-dependent endocytosis, clathrin- and caveolae-independent pathways, or passive diffusion. In contrast, larger particles (200 nm–5 μm) are mainly internalized via phagocytosis or macropinocytosis. Phagocytosis is chiefly performed by specialized immune cells, including macrophages, monocytes, neutrophils, and dendritic cells, which are responsible for defense and clearance of cellular debris and pathogens. Macropinocytosis is a unique form of endocytosis where large volumes of extracellular fluid are internalized into sizable

vesicles called macropinosomes, facilitated by actin-dependent membrane protrusions [51,52]. Additionally, the cell membrane is generally negatively charged due to its phospholipid bilayer. Positively charged nanoparticles tend to have a higher affinity for this negatively charged surface through electrostatic interactions, which enhances their binding and subsequent uptake [53]. In this study, the PBAE-plasmid NPs are approximately 500 nm in diameter. Given the cationic nature of PBAE polymers, which impart a positive charge to the nanoparticles, it is likely that their primary mode of cell entry is through macropinocytosis, driven by electrostatic attraction that promotes stronger interaction with the cell membrane and facilitates internalization.

3.5. Mitigation of DNCB-induced AD by MN patch

To examine the therapeutic efficacy of the MN patch for treating AD, we established a DNCB-induced AD mouse model (Fig. 5a). During the experiment, the MN treatment did not lead to a significant reduction in the mice's body weight ($p > 0.05$), indicating that it has no negative impact on their growth (Fig. 5b). Furthermore, the serum levels of nephrotoxicity indicators (creatinine, urea, and uric acid) and

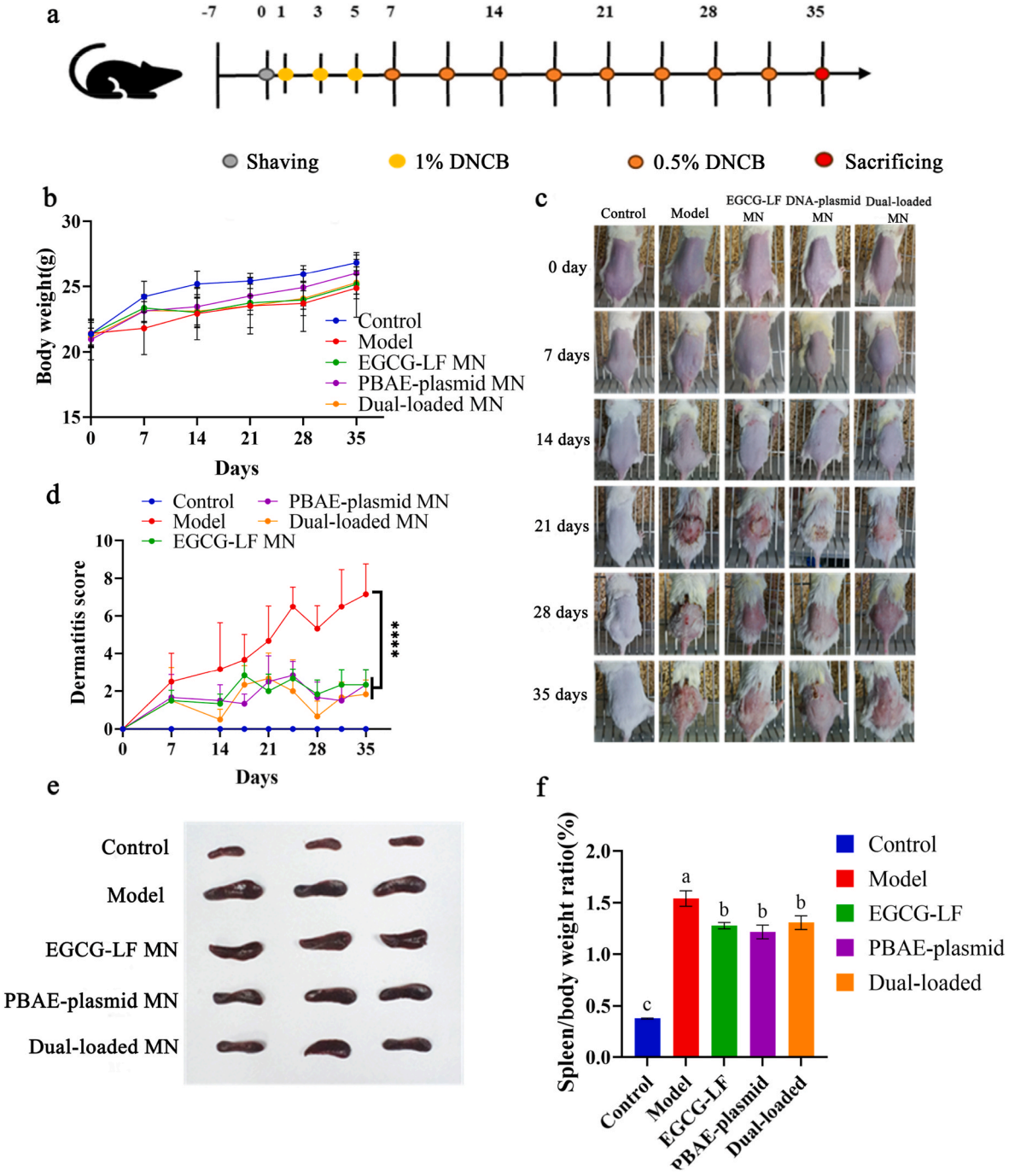

Fig. 5. Mitigation of DNCB-induced AD by the MN Patches. (**a**) Schematic illustration of the MN patches for the treatment of DNCB-induced AD. (**b**) Changes in body weight throughout the experiment. (**c**) Photographs of mice treated with MN patches on days 0, 7, 14, 21, 28, and 35. (**d**) Dermatitis severity scores of mice in different treatment groups. (**e**) Representative gross photograph of the spleens on day 35. (**f**) Spleen index of mice treated with MN patches on day 35. Data are presented as mean ± SD (n = 6). Bars sharing the same letter are not significantly different, whereas those with different letters are statistically significant ($p < 0.05$). ****$p < 0.0001$.

hepatotoxicity indicators (alanine aminotransferase and aspartate aminotransferase) in the treated AD mice were comparable to those in the untreated AD mice (Fig. S5). These findings indicate the safety and potential suitability of the MN patch for transdermal applications *in vivo*.

To assess the severity of skin damage in the AD mouse model, we quantitatively evaluated skin conditions based on four common indicators: edema, desquamation/dryness, erythema/hemorrhage, and ulceration/exfoliation [54]. As shown in Fig. 5c–d, DNCB-induced mice exhibited clear AD-like symptoms. By day 7, the skin lesion score in the model group averaged 2.50 ± 1.52, significantly greater than that of the control group. Over the course of 14 days, model mice displayed edema, noticeable erythema, hemorrhage, dryness, and desquamation. By day 21, severe erythema, hemorrhage, ulceration, and exfoliation were documented in the model group. Treatment with MN patches loaded with EGCG-LF NPs, PBAE-plasmid NPs, or their combinations significantly mitigated AD symptoms throughout the experiment. By day 35, the skin damage severity score in the model group reached 7.17 ± 1.60, while the scores of the three MN-treated groups were around 2 ($p < 0.0001$). Notably, the group treated with dual-loaded MN patches showed the lowest skin damage severity score of 1.83 ± 0.75. AD is characterized as an autoimmune disease, and the spleen-to-body weight ratio serves as a valuable biomarker for assessing immune function, health status, and the body's response to diseases [55]. As shown in Fig. 5e–f, the control group had small spleens, resulting in a spleen-to-body weight ratio of 0.38 ± 0.02. In contrast, the model mice exhibited significantly enlarged spleens, with an increased spleen-to-body weight ratio of 1.54 ± 0.18. Notably, a significant decrease in the spleen-to-body weight ratio was observed in mice treated with all three MN patches, indicating an improvement in immune function.

A previous investigation demonstrated that oral consumption of EGCG (100 mg/kg) could significantly alleviate AD-like skin phenotypes in DNFB-treated mice through the AGE-RAGE signaling pathway [56]. In another work, EGCG-based carbon dots (EGCG@CDs) were developed and encapsulated in an alginate hydrogel (ALG) for AD treatment. These carbon dots effectively scavenged reactive oxygen species (ROS), produced hydrogen peroxide to inhibit bacterial growth, and reduced mast cell activation [57]. However, the dermatitis scores of the treated mice decreased to only about 50% of those in the model group in both studies. The therapeutic benefits of topical JAK inhibitors are suboptimal. Their effectiveness is constrained due to the necessity for high threshold doses and low skin reservoir levels, limiting their efficacy as topical treatments for AD. For instance, the overall success rates for 0.75% and 1.5% ruxolitinib cream after eight weeks of treatment were approximately 50%, based on the Investigator's Global Assessment treatment success (IGA-TS) scores [58,59]. In this study, the three developed MN patches for AD treatment demonstrated marked improvement (approximately 75%) in therapeutic efficacy, as assessed by skin lesion severity scores in a murine AD model. It is important to note that murine scoring systems are fundamentally different from standardized clinical endpoints like the IGA-TS, and thus, the results cannot be directly equated to human outcomes. Despite this distinction, the pronounced therapeutic efficacy observed underscores the significant translational potential of these patches and strongly supports further clinical investigation.

3.6. Histological examination of skin tissue from AD mice after MN patch treatment

Epidermal hyperplasia is a common characteristic observed in many patients with AD [54]. H&E staining provided an overview of the mouse skin, revealing the normal epidermal and dermal structures in the control group. The stratum basale, stratum spinosum, and stratum granulosum were organized, and the hair follicles, sebaceous glands, and other normal structures were intact. In contrast, the model mice exhibited acanthosis and dermal edema, along with marked infiltration of inflammatory cells. Treatment with MN patches loaded with EGCG-LF NPs, PBAE-plasmid NPs, or both formulations resulted in significant improvements in skin epithelium health (Fig. 6a). The epidermal thickness in the model group (163.12 ± 22.54 μm) was significantly greater than that in the control group (28.10 ± 2.47 μm). All three MN patch treatments significantly reduced epidermal thickness ($p < 0.05$). Notably, the dual-loaded MN patch group showed the most substantial reduction, with an average epidermal thickness of 75.38 ± 7.74 μm (Fig. 6b).

Mast cell infiltration is another key pathophysiological feature of AD. The activation of mast cells, through IgE cross-linking on high-affinity receptors, results in the release of histamine and other chemokines, promoting T cell polarization toward the Th2 phenotype and triggering inflammatory responses [60,61]. Collagen, a primary component of the extracellular matrix, plays a crucial role in maintaining the structural integrity of healthy skin. Skin barrier dysfunction in AD patients is often linked to reduced collagen deposition, making decreased collagen content an indicator of AD development or severity [62]. As shown in Fig. 6c–f, the model group exhibited a significant increase in mast cell numbers and a notable reduction in collagen content compared to the control group. Treatment with the three MN patches led to a remarkable decrease in mast cell counts and restored collagen content in mouse skin ($p < 0.05$). The dual-loaded MN patch treatment demonstrated a slight advantage in reducing mast cell counts. These results suggested that the dual-loaded MN patch might have a slightly better effect on reducing inflammation compared to MN patch loaded with either single NPs.

3.7. Regulation of MN patches on the inflammation, JAK1 and Nrf2/HO-1 pathways

The regulation of AD includes the release of various cytokines by immune cells, keratinocytes, and other cell types. Th1 and Th2 responses refer to two distinct immune pathways involved in inflammatory skin diseases, each marked by the release of specific cytokines. In the acute phases of these conditions, Th2-type cytokines such as IL-33, IL-31, IL-13, and IL-4 predominate. Conversely, during the chronic phase of AD, Th1 responses take center stage, characterized by the production of cytokines like IFN-γ, TNF-α, and IL-1β [63]. These cytokines subsequently activate B cells to generate IgE, which further contributes to the buildup of eosinophils and mast cells (MCs) in AD lesions. This process escalates the release of inflammatory mediators and worsens the symptoms of the condition [64–66]. The elevated serum total IgE level is a characteristic feature of the immune environment in AD [67]. As illustrated in Fig. 7a–e, the model group demonstrated significantly higher tissue levels of IL-1β, IL-4, IL-13, and along with increased serum levels of TSLP and IgE, compared to the control group ($p < 0.05$). Treatment with MN patches loaded with single or double NPs reduced these levels, with the dual-loaded MN patches demonstrating greater efficacy against IL-1β ($p < 0.05$). This cytokine serves as a crucial mediator in the development of an AD phenotype by inducing TSLP and disrupting epidermal homeostasis [68].

Targeting the JAK/STAT pathway has proven effective in regulating immune cell responses, oxidative stress, and skin barrier function, establishing it as a crucial therapeutic target for AD [69]. Modulating the JAK/STAT pathway has been shown to enhance the maturation and differentiation of B cells into plasma cells, which subsequently leads to the secretion of IgE. Additionally, this pathway can activate skin mast cells, promoting the release of histamine and directly influencing mast cell homeostasis and proliferation [70]. Inhibition of the JAK1/STAT3 signaling pathway has been identified as a key mechanism by which N-heterocyclic functionalized chalcone derivatives and the traditional Chinese medicine (TCM) Jiu-Wei-Yong-An (JWYA) formula alleviate AD-like skin lesions [63,71]. Furthermore, momelotinib, a JAK1/JAK2 inhibitor, has been reported to reduce serum IgE levels by inhibiting STAT3 phosphorylation, thereby decreasing inflammatory responses in a DNCB-induced AD model in mice [69]. As illustrated in Fig. 7f–g, the skin tissue of mice in the model group demonstrated significantly higher

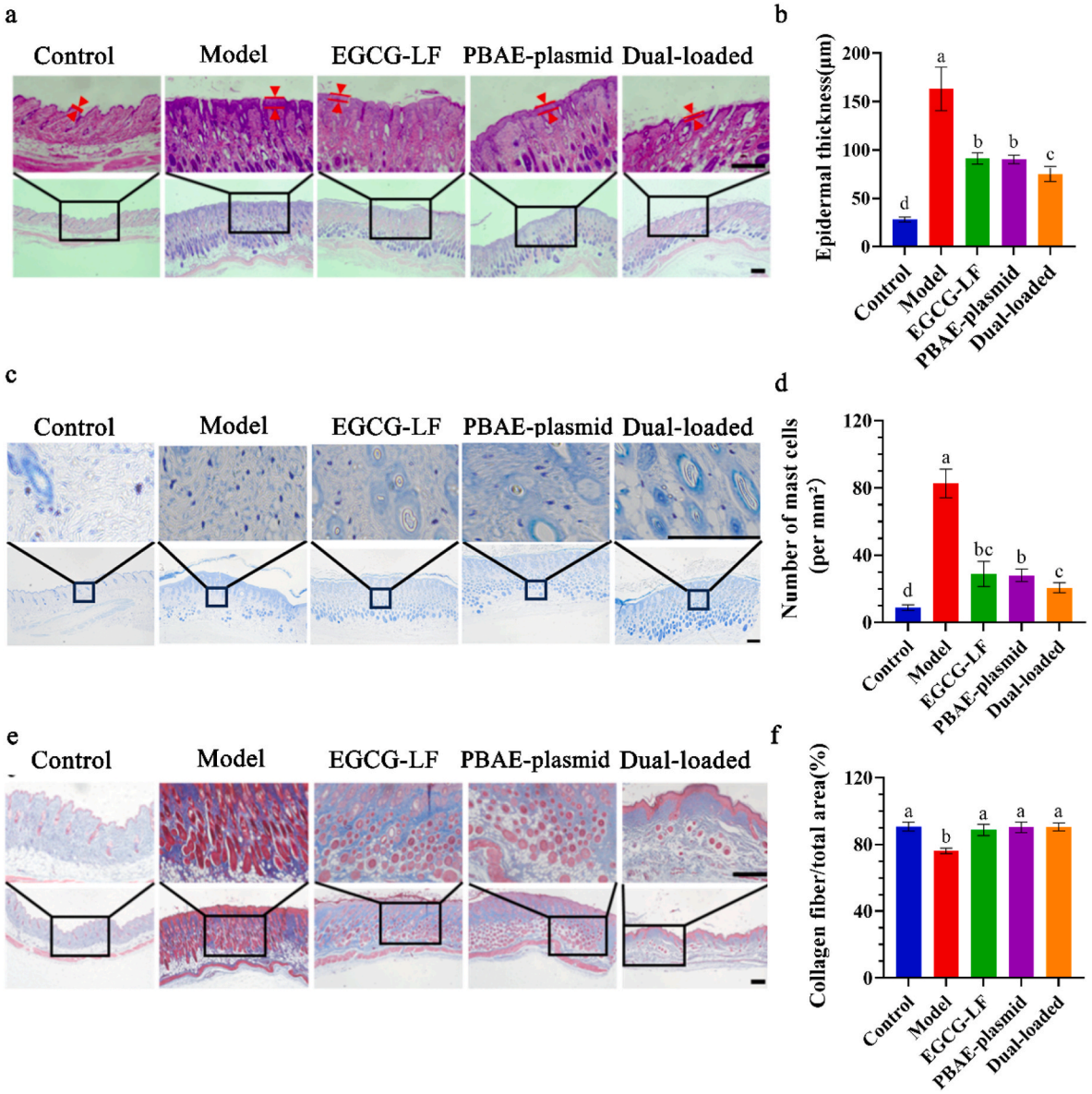

Fig. 6. Histological analysis of skin tissue from AD mice treated with MN patches. (**a**) H&E staining of dorsal skin sections of mice. (**b**) Quantitative analysis of epidermal thickness in H&E-stained microphotographs. (**c**) Mast cell staining in dorsal skin sections of mice. (**d**) Quantitative analysis of mast cell numbers in mast cell-stained microphotographs. (**e**) Masson staining of dorsal skin sections of mice. (**f**) Quantitative analysis of collagen fibers in Masson-stained microphotographs. Scale bar = 300 μm. Data are presented as mean ± SD (n = 6). Bars sharing the same letter are not significantly different, whereas those with different letters are statistically significant ($p < 0.05$).

levels of JAK1 compared to the control group ($p < 0.05$). Treatment with MN patches containing PBAE-plasmid NPs, or both types of NPs, significantly reduced JAK1 protein expression ($p < 0.05$). Notably, the dual-loaded MN patches exhibited a greater inhibitory effect on JAK1 expression than the other two MN patch types ($p < 0.05$). EGCG has been reported to inhibit melanoma growth by targeting the JAK-STAT signaling pathway [72]. The synergistic effects of EGCG and gene editing explain the enhanced regulatory impact of the dual-loaded MN patches on JAK1.

Clinicopathological data from patients with AD consistently demonstrate increased levels of ROS and oxidative stress markers, indicating the significant role of oxidative stress in AD pathogenesis. Among these markers, 8-OHdG is closely associated with AD and serves as an important indicator of DNA oxidative damage. 8-OHdG is generated when hydroxyl radicals attack the deoxyguanosine residue at the C-8 position in DNA, leading to oxidation [73]. The Nrf2/HO-1 signaling pathway plays a crucial role in various cellular defense mechanisms, including antioxidant responses, phase II detoxification, inflammatory signaling, and DNA repair, and is regarded as a protective mechanism against AD. Studies have shown that skin lacking Nrf2 is more prone to heightened inflammation associated with AD [74,75]. As illustrated in Fig. 7h, the model group showed elevated level of 8-OHdG in skin tissues compared to the control group. Treatment with the MN patch loaded with EGCG-LF NPs, as well as the dual-loaded MN patch, resulted in a significant reduction of 8-OHdG levels in mouse tissues ($p < 0.05$). Furthermore, their effects were stronger than that of the MN patch containing PBAE-plasmid NPs ($p < 0.05$). Fig. 7i–l illustrated that the expression levels of Nrf2 and HO-1 in the skin tissue of mice in the model group were significantly lower than those in the control group ($p < 0.05$). All three types of MN patches significantly reversed the expression of these two proteins, with the exception of the MN patch loaded with PBAE-plasmid NPs, which only induced a slight increase in the average HO-1 expression that was not statistically significant compared to the model group. EGCG can ameliorate oxidative stress,

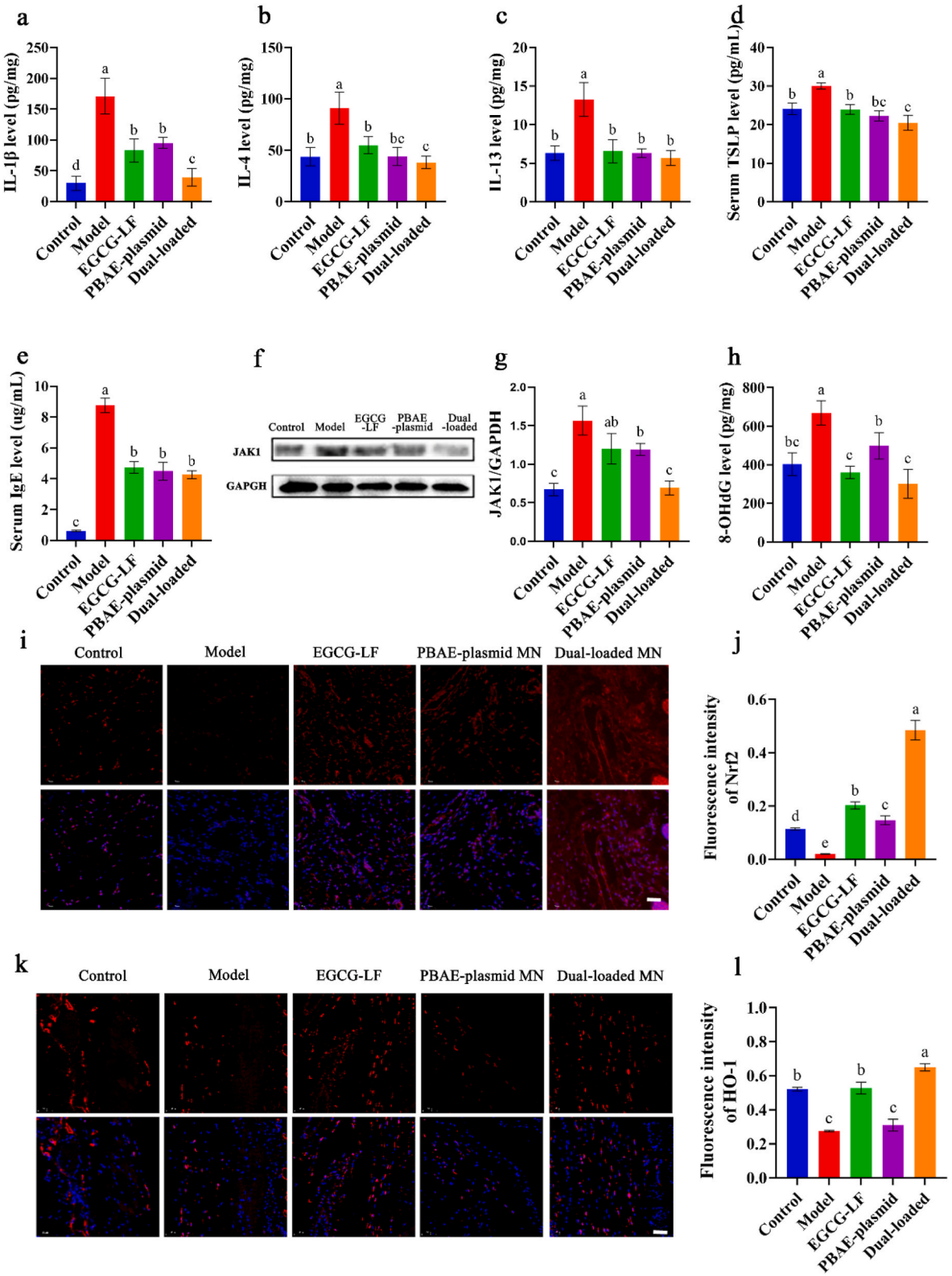

Fig. 7. Regulation of MN patches on the inflammation, JAK1 and Nrf2/HO-1 pathways in AD mice. (**a-c**) Levels of IL-1β, IL-4, and IL-13 in the dorsal skin. (**d, e**) Levels of TSLP and IgE in the serum. (**f**) Protein expression of JAK1 in the dorsal skin. (**g**) Quantitative analysis of JAK1 protein levels from (f). (**h**) 8-OHdG levels in the dorsal skin. (**i**) Fluorescent immunostaining of Nrf2, with the merged image showing DAPI staining (red: Nrf2, blue: DAPI). (**j**) Quantitative analysis of Nrf2 protein expression from (i). (**k**) Fluorescent immunostaining of HO-1, along with the merged image showing DAPI staining (red: HO-1, blue: DAPI). (**l**) Quantitative analysis of HO-1 protein expression from (k). Data are presented as mean ± SD (n = 6). Bars sharing the same letter are not significantly different, whereas those with different letters are statistically significant ($p < 0.05$).

inflammation, cell apoptosis, and ischemia-reperfusion injury by inhibiting the Nrf2/HO-1 signaling pathway in various tissues and cell types [76,77]. This explains why the MN patch loaded with EGCG-LF NPs exhibits better antioxidant activity and regulation of Nrf2 and HO-1 expression compared to the MN patch containing PBAE-plasmid NPs ($p < 0.05$). Compared to the model group, PBAE-plasmid NPs induced a significantly greater upregulation of Nrf2 than of HO-1. HO-1 expression is known to be regulated by a wide range of chemical and physical stimuli. In addition to Nrf2, its levels can be modulated by various transcription factors—such as BTB and CNC homology 1 (Bach-1), activator protein-1 (AP-1), heat shock factor-1 (HSF-1), and NF-κB—as well as by microRNAs (miRNAs). This complex regulatory network may underlie the differential expression of Nrf2 and HO-1 following PBAE-plasmid NP treatment. The underlying molecular mechanisms warrant further investigation [78–80]. The dual-loaded MN patch produced significantly greater Nrf2 activation than patches loaded with either single NPs ($p < 0.05$). It also induced a modest increase in HO-1 levels relative to the EGCG-LF NP-loaded patch ($p < 0.05$), and a substantial increase compared to the PBAE-plasmid NP-loaded patch ($p < 0.05$). Additionally, considering the above-mentioned effects on JAK1, this may explain its relatively large or modest enhanced ability to suppress inflammatory cytokines such as IL-1β, IL-4, and TSLP in AD mice.

Although AD is predominantly a Th2-skewed disorder, its pathogenesis is multifaceted and involves a broad array of immune cells, including keratinocytes, dendritic cells, macrophages, mast cells, innate lymphoid cells, granulocytes, monocytes, and various T cell subsets such as Th1, Th17, and Th22 [66]. Th2- and non-Th2–type proinflammatory cytokines contribute to disease initiation, a combination of Th1-, Th2-, and non-Th–type proinflammatory mediators participate in disease maintenance. IL-1β plays a role in the induction phase of AD, and controlling its activity may help prevent disease progression [81]. IL-1β expression has been observed to rise during AD flares and to decline when flares are managed with topical corticosteroids. Notably, IL-1β levels also appear to correlate with the initial severity of the disease [82]. Nrf2 is critical in preserving skin functions such as epidermal differentiation, regulating skin immunity, and managing environmental stresses. Besides, it plays an important role in the pathogenesis of common inflammatory skin diseases such as AD [83]. Impaired Nrf2 activation is linked to mitochondrial abnormalities in AD, collectively presenting potential targets for pharmacological intervention [84]. These findings suggest that, in addition to Th2-associated inflammatory mediators and pathways, other factors may also contribute to the amelioration of AD. In this study, both individual NPs and their combination demonstrated a significant suppressive effect on Th2-associated inflammation. Compared to the single NP treatment groups, the dual-loaded MN treatment demonstrated superior efficacy in reducing IL-1β and JAK1 levels and upregulating Nrf2 expression. However, it led to only marginal improvements in the Th2-related markers IL-4 and TSLP, and no significant reduction in IL-13 or IgE. These results indicated that the enhanced therapeutic efficacy of the combination treatment is likely mediated through mechanisms independent of the Th2 pathway, which warrants further investigation in future studies.

3.8. Limitations and future directions

Several limitations in this study warrant further consideration. First, the research was conducted using a mouse model, which may not fully replicate human physiological and pathological conditions. To more accurately assess the efficacy of this microneedle nanomedicine system, larger animal models—such as dogs or pigs—that share greater anatomical and physiological similarities to humans in terms of size, lifespan, and tissue structure should be employed. Second, the plasmid particles used for gene editing are relatively large and differ significantly in size from the EGCG-LF NPs, potentially impairing the co-delivery efficiency of the two therapeutic agents. Future research should focus on optimizing the design of cationic polymers and transfection vectors to further reduce the size of the gene delivery system, thereby enhancing overall therapeutic performance [85,86]. Third, although macropinocytosis is the most probable uptake mechanism for the PBAE-plasmid NPs, our current study did not employ pathway-specific inhibitors to quantify the contribution of macropinocytosis relative to other endocytic routes. Future investigations incorporating endocytosis pathway inhibitors or genetic perturbations would be valuable for precisely mapping the uptake mechanisms and optimizing nanocarrier design for targeted trafficking. Fourth, while this study demonstrates the modulation of key signaling components JAK1 and Nrf2, it does not provide a comprehensive analysis of their critical downstream effectors and interacting partners. This includes members of the STAT family, suppressors of cytokine signaling (SOCS) proteins for the JAK1 pathway, and key regulators like Kelch-like ECH-associated protein 1 (KEAP1) or the binding to antioxidant response elements (ARE) for the Nrf2 pathway. Furthermore, potential crosstalk between the JAK1 and Nrf2 pathways, which could significantly influence the observed anti-inflammatory and antioxidant outcomes, remains unexplored. Future studies should aim to characterize these broader signaling networks and interactions to fully elucidate the molecular mechanisms underlying the therapeutic potential identified here. Fifth, the application of CRISPR-based gene silencing carries inherent risks of off-target effects and unintended genetic modifications [87]. Additionally, the potential for nanoparticle materials to elicit local or systemic immune responses remains largely unexplored. Consequently, further clinical trials are necessary to thoroughly evaluate safety and efficacy before translating these findings into human therapies.

4. Conclusion

We developed a MN patch transdermal delivery system that combines EGCG- LF NPs with the CRISPR/CasRx system targeting JAK1 for the treatment of AD. The self-assembled EGCG-LF NPs exhibited lower cytotoxicity, enhanced stability and efficacy in alleviating oxidative stress, along with a higher cellular uptake efficiency for EGCG, compared to its free form. Additionally, the PBAE-plasmid NPs achieve significant knockdown of JAK1 expression both i*n vitro* and *in vivo*. In animal experiments, the MN patch loaded with EGCG-LF NPs and PBAE-plasmid NPs rapidly dissolves upon insertion into the dorsal skin of mice, ensuring efficient drug release. Patches loaded with either single NPs or both NPs effectively alleviated dermatitis symptoms in mice with DNCB-induced AD, exhibiting excellent biosafety, antioxidant properties, and anti-inflammatory effects that promote skin barrier repair. The dual-loaded MN patch showed slight improvement in epidermal thickness, mast cell counts, IL-4, TSLP, 8-OHdG, and HO-1 compared to the single-agent groups, and demonstrated a more pronounced enhancement in modulating IL-1β, JAK1, and Nrf2 levels. In conclusion, our study highlights the promising potential of microneedle administration of EGCG-loaded natural product nanomedicines and gene-edited nanomedicines for managing AD.

CRediT authorship contribution statement

Huanqing Zhu: Formal analysis, Investigation, Methodology, Visualization, Writing – original draft. **Haonan Yu:** Data curation, Formal analysis, Validation, Visualization. **Mengxin Huang:** Investigation, Validation. **Panjie Sun:** Investigation, Validation. **Yuanfang Tang:** Investigation, Validation. **Zhanyi Zhang:** Investigation, Validation. **Puming He:** Resources, Supervision. **Youying Tu:** Resources, Supervision. **Bo Li:** Conceptualization, Funding acquisition, Project administration, Writing – review & editing.

Declaration of competing interest

The authors declare that they have no known competing financial

interests or personal relationships that could have appeared to influence the work reported in this paper.

Acknowledgements

This work was supported by the Key Research and Development Program of Zhejiang Province (2023C02041), and National Natural Science Foundation of China (32272303). We thank Prof. Yuan Ping at Zhejiang University for providing technical assistance.

Appendix. ASupplementary data

Supplementary data to this article can be found online at https://doi.org/10.1016/j.mtbio.2026.102884.

Data availability

Data will be made available on request.

References

[1] T. Bieber, Atopic dermatitis: an expanding therapeutic pipeline for a complex disease, Nat. Rev. Drug Discov. 21 (1) (2022) 21–40, https://doi.org/10.1038/s41573-021-00266-6.
[2] M. Kim, H.J. Yuk, Y. Min, D.S. Kim, Y.Y. Sung, Extract alleviates atopy-like lesions in NC/Nga mice via inhibition of the JAK1-STAT1/3 pathway, Biomed. Pharmacother. 169 (2023) 115903, https://doi.org/10.1016/j.biopha.2023.115903.
[3] S. Weidinger, L.A. Beck, T. Bieber, K. Kabashima, A.D. Irvine, Atopic dermatitis, Nat. Rev. Dis. Primers 4 (2018) 1, https://doi.org/10.1038/s41572-018-0001-z.
[4] I.H. Huang, W.H. Chung, P.C. Wu, C.B. Chen, JAK-STAT signaling pathway in the pathogenesis of atopic dermatitis: an updated review, Front. Immunol. 13 (2022) 1068260, https://doi.org/10.3389/fimmu.2022.1068260.
[5] S. Ferreira, E. Guttman-Yassky, T. Torres, Selective JAK1 inhibitors for the treatment of atopic dermatitis: focus on upadacitinib and abrocitinib, Am. J. Clin. Dermatol. 21 (6) (2020) 783–798, https://doi.org/10.1007/s40257-020-00548-6.
[6] R. Chovatiya, A.S. Paller, JAK inhibitors in the treatment of atopic dermatitis, J. Allergy Clin. Immunol. 148 (4) (2021) 927–940, https://doi.org/10.1016/j.jaci.2021.08.009.
[7] D.G. Cotter, D. Schairer, L. Eichenfield, Emerging therapies for atopic dermatitis: JAK inhibitors, J. Am. Acad. Dermatol. 78 (3) (2018) S53–S62, https://doi.org/10.1016/j.jaad.2017.12.019.
[8] S. Yoon, K. Kim, K. Shin, H.S. Kim, B. Kim, M.B. Kim, et al., The safety of systemic janus kinase inhibitors in atopic dermatitis: a systematic review and meta-analysis of randomized controlled trials, J. Eur. Acad. Dermatol. 38 (1) (2024) 52–61, https://doi.org/10.1111/jdv.19426.
[9] N. Healey, Next-generation CRISPR-based gene-editing therapies tested in clinical trials, Nat. Med. 30 (9) (2024) 2380–2381, https://doi.org/10.1038/d41591-024-00056-8.
[10] T.W. Li, L.S. Zhang, T. Lu, T.M. Zhu, C.B. Feng, N. Gao, et al., Engineered extracellular vesicle-delivered CRISPR/CasRx as a novel RNA editing tool, Adv. Sci. 10 (10) (2023) 2206517, https://doi.org/10.1002/advs.202206517.
[11] Y.Q. Lin, C.J. Li, Y.Z. Chen, J.L. Gao, J.W. Li, C.H. Huang, et al., RNA-targeting CRISPR/CasRx system relieves disease symptoms in Huntington'S disease models, Mol. Neurodegener. 20 (1) (2025) 4, https://doi.org/10.1186/s13024-024-00794-w.
[12] D.P. McLornan, J.E. Pope, J. Gotlib, C.N. Harrison, Current and future status of JAK inhibitors, Lancet 398 (10302) (2021) 803–816, https://doi.org/10.1016/S0140-6736(21)00438-4.
[13] T.S. He, W.L. Tang, J.L. Chen, J.L. Xie, Z.Z. Weng, D. Deng, et al., Hydrogel-based treatment of house dust mite-induced atopic dermatitis through triple cleaning of mites, bacteria, and ROS-related inflammation, ACS Appl. Mater. Interfaces 16 (26) (2024) 33121–33134, https://doi.org/10.1021/acsami.4c05435.
[14] Y.B. Jia, J.H. Hu, K.L. An, Q. Zhao, Y. Dang, H. Liu, et al., Hydrogel dressing integrating FAK inhibition and ROS scavenging for mechano-chemical treatment of atopic dermatitis, Nat. Commun. 14 (1) (2023) 2478, https://doi.org/10.1038/s41467-023-38209-x.
[15] G. Messire, R. Serreau, S. Berteina-Raboin, Antioxidant effects of catechins (EGCG), andrographolide, and curcuminoids compounds for skin protection, cosmetics, and dermatological uses: an update, Antioxidants 12 (7) (2023) 1317, https://doi.org/10.3390/antiox12071317.
[16] S.U. Noh, E.A. Cho, H.O. Kim, Y.M. Park, Epigallocatechin-3-gallate improves extract-induced atopic dermatitis-like skin lesions in NC/Nga mice by suppressing macrophage migration inhibitory factor, Int. Immunopharmacol. 8 (9) (2008) 1172–1182, https://doi.org/10.1016/j.intimp.2008.04.002.
[17] Q.Q. Yang, X.L. Wei, Y.P. Fang, R.Y. Gan, M. Wang, Y.Y. Ge, et al., Nanochemoprevention with therapeutic benefits: an updated review focused on epigallocatechin gallate delivery, Crit. Rev. Food Sci. 60 (8) (2020) 1243–1264, https://doi.org/10.1080/10408398.2019.1565490.
[18] A.V.P. Silvestrini, M.F. Morais, B.W. Debiasi, F.G. Praça, M.V.L.B. Bentley, Nanotechnology strategies to address challenges in topical and cellular delivery of siRNAs in skin disease therapy, Adv. Drug Deliv. Rev. 207 (2024) 115198, https://doi.org/10.1016/j.addr.2024.115198.
[19] A.O. Elzoghby, M.A. Abdelmoneem, I.A. Hassanin, M.M. Abd Elwakil, M. A. Elnaggar, S. Mokhtar, et al., Lactoferrin, a multi-functional glycoprotein: active therapeutic, drug nanocarrier & targeting ligand, Biomaterials 263 (2020) 120355, https://doi.org/10.1016/j.biomaterials.2020.120355.
[20] L.H. Li, L.W. Tan, Q. Zhang, Y.S. Cheng, Y.Y. Liu, R. Li, et al., Nose-to-brain delivery of self-assembled curcumin-lactoferrin nanoparticles: characterization, neuroprotective effect and pharmacokinetic study, Front. Bioeng. Biotechnol. 11 (2023) 1168408, https://doi.org/10.3389/fbioe.2023.1168408.
[21] Y.S. Wang, M. Ji, M.J. Xing, A.X. Bao, D.L. Wang, L. Li, et al., Effects of ultrasound and thermal treatment on the interaction between hyaluronic scid and lactoferrin: preparation, structures and functionalities, Int. J. Biol. Macromol. 272 (2024) 132812, https://doi.org/10.1016/j.ijbiomac.2024.132812.
[22] X.Y. Hong, Z.Z. Wu, L.Z. Chen, F. Wu, L.M. Wei, W.E. Yuan, Hydrogel microneedle arrays for transdermal drug delivery, Nano-Micro Lett. 6 (3) (2014) 191–199, https://doi.org/10.1002/adfm.201200864.
[23] Q. Ul Ain, E.V.R. Campos, A. Huynh, D. Witzigmann, S. Hedtrich, Gene delivery to the skin - how far have we come? Trends, Biotechnol. 39 (5) (2021) 474–487, https://doi.org/10.1016/j.tibtech.2020.07.012.
[24] H.H. Wessels, A. Méndez-Mancilla, X.Y. Guo, M. Legut, Z. Daniloski, N.E. Sanjana, Massively parallel cas13 screens reveal principles for guide RNA design, Nat. Biotechnol. 38 (6) (2020) 722, https://doi.org/10.1038/s41587-020-0456-9.
[25] X.J. Yan, Q. Pan, H.H. Xin, Y.X. Chen, Y. Ping, Genome-editing prodrug: targeted delivery and conditional stabilization of CRISPR-Cas9 for precision therapy of inflammatory disease, Sci. Adv. 7 (50) (2021) eabj0624, https://doi.org/10.1126/sciadv.abj0624.
[26] T. Liu, M. Liu, H. Liu, Y. Ren, Y. Zhao, H. Yan, et al., Co-encapsulation of (-)-epigallocatechin-3-gallate and piceatannol/oxyresveratrol in β-lactoglobulin: effect of ligand-protein binding on the antioxidant activity, stability, solubility and cytotoxicity, Food Funct. 12 (16) (2021) 7126–7144, https://doi.org/10.1039/d1fo00481f.
[27] T. Dyrda-Terniuk, P. Pomastowski, The multifaceted roles of bovine lactoferrin: molecular structure, isolation methods, analytical characteristics, and biological properties, J. Agric. Food Chem. 71 (51) (2023) 20500–20531, https://doi.org/10.1021/acs.jafc.3c06887.
[28] F.G. Liu, S.H. Zhang, J.Y. Li, D.J. McClements, X.B. Liu, Recent development of lactoferrin-based vehicles for the delivery of bioactive compounds: complexes, emulsions, and nanoparticles, Trends Food Sci. Technol. 79 (2018) 67–77, https://doi.org/10.1016/j.tifs.2018.06.013.
[29] S. Kim, S.Y. Hong, H. Jeong, J. Lee, K. Park, H. Joo, et al., Lactoferrin-polyphenol composite nanocoating with enhanced chemical stability and cell-compatibility, Prog. Org. Coating 187 (2024) 108099, https://doi.org/10.1517/17425247.2011.615829.
[30] V.S. Bollimpelli, P. Kumar, S. Kumari, A.K. Kondapi, Neuroprotective effect of curcumin-loaded lactoferrin nano particles against rotenone induced neurotoxicity, Neurochem. Int. 95 (2016) 37–45, https://doi.org/10.1016/j.neuint.2016.01.006.
[31] Z.H. Zhang, X.P. Wang, W.Y. Ayman, W.L.L. Munyendo, H.X. Lv, J.P. Zhou, Studies on lactoferrin nanoparticles of gambogic acid for oral delivery, Drug Deliv. 20 (2) (2013) 86–93, https://doi.org/10.3109/10717544.2013.766781.
[32] B. Li, W.K. Du, J.C. Jin, Q.Z. Du, Preservation of (-)-epigallocatechin-3-gallate antioxidant properties loaded in heat treated β-lactoglobulin nanoparticles, J. Agric. Food Chem. 60 (13) (2012) 3477–3484, https://doi.org/10.1021/jf300307t.
[33] J.H. Lee, J.Y. Lim, E.H. Jo, H.M. Noh, S. Park, M.C. Park, et al., Chijabyukpi-tang inhibits pro-inflammatory cytokines and chemokines the Nrf2/HO-1 signaling pathway in TNF-α/IFN-γ-stimulated HaCaT cells and ameliorates 2,4-dinitro-chlorobenzene-Induced atopic dermatitis-like skin lesions in mice, Front. Pharmacol. 11 (2020) 1018, https://doi.org/10.3389/fphar.2020.01018.
[34] D.S. Hsieh, H. Wang, S.W. Tan, Y.H. Huang, C.Y. Tsai, M.K. Yeh, et al., The treatment of bladder cancer in a mouse model by epigallocatechin-3-gallate-gold nanoparticles, Biomaterials 32 (30) (2011) 7633–7640, https://doi.org/10.1016/j.biomaterials.2011.06.073.
[35] C.C. Li, L. Chen, D.J. McClements, X.W. Peng, Z.L. Xu, M. Meng, et al., Encapsulation of polyphenols in protein-based nanoparticles: preparation, properties, and applications, Crit. Rev. Food Sci. Nutr. 64 (31) (2024) 11341–11355, https://doi.org/10.1080/10408398.2023.2237126.
[36] Y.E. Kim, S.W. Choi, M.K. Kim, T.L. Nguyen, J. Kim, Therapeutic hydrogel patch to treat atopic dermatitis by regulating oxidative stress, Nano Lett. 22 (5) (2022) 2038–2047, https://doi.org/10.1021/acs.nanolett.1c04899.
[37] G.P. Chen, Y.Y. Wang, X.B. Liu, F.G. Liu, Enhancing the effects of curcumin on oxidative stress injury in brain vascular endothelial cells using lactoferrin peptide nano-micelles: antioxidant activity and mechanism, J. Sci. Food Agric. 105 (1) (2025) 372–381, https://doi.org/10.1002/jsfa.13836.
[38] R. Raychaudhuri, A. Pandey, S. Das, S.H. Nannuri, A. Joseph, S.D. George, et al., Nanoparticle impregnated self-supporting protein gel for enhanced reduction in oxidative stress: a molecular dynamics insight for lactoferrin-polyphenol interaction, Int. J. Biol. Macromol. 189 (2021) 100–113, https://doi.org/10.1016/j.ijbiomac.2021.08.089.
[39] Z. Esmaeili, P.S. Gilani, M. Khosravani, M. Motamedi, S. Maleknejad, M. Adabi, et al., Nanotechnology-driven EGCG: bridging antioxidant and therapeutic roles in metabolic and cancer pathways, Nanomedicine-UK 20 (6) (2025) 621–636, https://doi.org/10.1080/17435889.2025.2462521.

[40] K. Reich, J.P. Thyssen, A. Blauvelt, K. Eyerich, W. Soong, Z.P. Rice, et al., Efficacy and safety of abrocitinib versus dupilumab in adults with moderate-to-severe atopic dermatitis: a randomised, double-blind, multicentre phase 3 trial, Lancet 400 (10348) (2022) 273–282, https://doi.org/10.1016/S0140-6736(22)01199-0.
[41] S. Konermann, P. Lotfy, N.J. Brideau, J. Oki, M.N. Shokhirev, P.D. Hsu, Transcriptome engineering with RNA-targeting type VI-D CRISPR effectors, Cell 173 (3) (2018) 665, https://doi.org/10.1016/j.cell.2018.02.033.
[42] G. Niu, Z. Jin, C. Zhang, D. He, X.Q. Gao, C.M. Zou, et al., An effective vaginal gel to deliver CRISPR/Cas9 system encapsulated in poly (β-amino ester) nanoparticles for vaginal gene therapy, EBioMedicine 58 (2020) 102897, https://doi.org/10.1016/j.ebiom.2020.102897.
[43] M. Gadina, JAK inhibitors: is specificity at all relevant? Semin. Arthritis Rheum. 64 (2024) 152327 https://doi.org/10.1016/j.semarthrit.2023.152327.
[44] B.H.J. Gowda, M.G. Ahmed, R.R.S. Thakur, R.F. Donnelly, L.K. Vora, Microneedles as an emerging platform for transdermal delivery of phytochemicals, Mol. Pharm. 21 (12) (2024) 6007–6033, https://doi.org/10.1021/acs.molpharmaceut.4c00894.
[45] T. Wan, Q. Pan, Y. Ping, Microneedle-assisted genome editing: a transdermal dtrategy of targeting by CRISPR-Cas9 for synergistic therapy of inflammatory skin disorders, Sci. Adv. 7 (11) (2021) eabe2888, https://doi.org/10.1126/sciadv.abe2888.
[46] S.Y. Ruan, J.Q. Li, H. Ruan, Q. Xia, X.L. Hou, Z. Wang, et al., Microneedle-mediated nose-to-brain drug delivery for improved Alzheimer'S disease treatment, J. Contr. Release 366 (2024) 712–731, https://doi.org/10.1016/j.jconrel.2024.01.013.
[47] H.M. Guo, H.M. Yuan, Y.R. Yu, J.W. Sun, Y. Sun, Y. Tang, et al., Role of skin-homing t-cells in recurrent episodes of atopic dermatitis: a review, Front. Immunol. 16 (2025) 1489277, https://doi.org/10.3389/fimmu.2025.1489277.
[48] H.K. Song, H.J. Kim, S.C. Kim, T. Kim, Therapeutic effects of Sigesbeckia pubescens Makino against atopic dermatitis-like skin inflammation through the JAK2/STAT signaling pathway, Int. J. Mol. Sci. 26 (9) (2025) 4191, https://doi.org/10.3390/ijms26094191.
[49] I. Saha, V.K. Rai, Hyaluronic acid based microneedle array: recent applications in drug delivery and cosmetology, Carbohydr. Polym. 267 (2021) 118168, https://doi.org/10.1016/j.carbpol.2021.118168.
[50] M. Al-Sibani, A. Al-Harrasi, R.H.H. Neubert, Effect of hyaluronic acid initial concentration on cross-linking efficiency of hyaluronic acid-based hydrogels used in biomedical and cosmetic applications, Pharmazie 72 (2) (2017) 81–86, https://doi.org/10.1691/ph.2017.6133.
[51] S. Behzadi, V. Serpooshan, W. Tao, M.A. Hamaly, M.Y. Alkawareek, E.C. Dreaden, et al., Cellular uptake of nanoparticles: journey inside the cell, Chem. Soc. Rev. 46 (14) (2017) 4218, https://doi.org/10.1039/c6cs00636a.
[52] J. Mosquera, I. García, L.M. Liz-Marzán, Cellular uptake of nanoparticles versus small molecules: a matter of size, Accounts Chem. Res. 51 (9) (2018) 2305, https://doi.org/10.1021/acs.accounts.8b00292.
[53] J. Zhang, R.R. Liu, Z. Yang, C.H. Luo, J.Y. Chen, B.L. Guo, et al., Physicochemical and surface properties of nanoparticles: effects on cellular pathway and uptake, ChemNanoMat (2025), https://doi.org/10.1002/cnma.202500043.
[54] B. Sanjel, W.S. Shim, The contribution of mouse models to understanding atopic dermatitis, Biochem. Pharmacol. 203 (2022) 115177, https://doi.org/10.1016/j.bcp.2022.115177.
[55] Y.H.A. Elewa, O. Ichii, Y. Kon, Comparative analysis of mediastinal fat-associated lymphoid cluster development and lung cellular infiltration in murine autoimmune disease models and the corresponding normal control strains, Immunology 147 (1) (2016) 30–40, https://doi.org/10.1111/imm.12539.
[56] L. Tang, T.S. Wang, R.Z. Peng, J.Y. Guo, L.P. Li, B.H. Zhou, et al., Mechanistic evaluation of EGCG against atopic dermatitis: an and study, Nat. Prod. Commun. 19 (12) (2024), https://doi.org/10.1111/imm.12539.
[57] J. Han, S. Choi, J. Hong, D. Gang, S. Lee, K. Shin, et al., Superoxide dismutase-mimetic polyphenol-based carbon dots for multimodal bioimaging and treatment of atopic dermatitis, ACS Appl. Mater. Interfaces 16 (19) (2024) 24308–24320, https://doi.org/10.1021/acsami.4c02634.
[58] T. Ju, A. Labib, A. Vander Does, G. Yosipovitch, Topical janus kinase-signal transducers and activators of transcription inhibitor tofacitinib is effective in reducing nonatopic dermatitis chronic itch: a case series, J. Am. Acad. Dermatol. 87 (2) (2022) 400–403, https://doi.org/10.1016/j.jaad.2022.03.012.
[59] K. Papp, J.C. Szepietowski, L. Kircik, D. Toth, L.F. Eichenfield, D.Y.M. Leung, et al., Efficacy and safety of ruxolitinib cream for the treatment of atopic dermatitis: results from 2 phase 3, randomized, double-blind studies, J. Am. Acad. Dermatol. 85 (4) (2021) 863–872, https://doi.org/10.1016/j.jaad.2021.04.085.
[60] S. Nakae, H. Suto, M. Kakurai, J.D. Sedgwick, M. Tsai, S.J. Galli, Mast cells enhance T cell activation: importance of mast cell-derived TNF, Proc. Natl. Acad. Sci. USA 102 (18) (2005) 6467–6472, https://doi.org/10.1073/pnas.0501912102.
[61] Y.X. Wang, S.S. Cao, K.Y. Yu, F.D. Yang, X.M. Yu, Y.H. Zhai, et al., Integrating tacrolimus into eutectic oil-based microemulsion for atopic dermatitis: simultaneously enhancing percutaneous delivery and treatment efficacy with relieving side effects, Int. J. Nanomed. 14 (2019) 5849–5863, https://doi.org/10.2147/IJN.S212260.
[62] O. Bhattacharjee, U. Ayyangar, A.S. Kurbet, D. Ashok, S. Raghavan, Unraveling the ECM-immune cell crosstalk in skin diseases, Front. Cell Dev. Biol. 7 (2019) 68, https://doi.org/10.3389/fcell.2019.00068.
[63] Q.W.F. Gu, J.C. Lin, X.L. Lu, T.R. Chen, Y.Y. Wu, Y.L. Yang, Jiu-Wei-Yong-an formula suppresses JAK1/STAT3 and MAPK signaling alleviates atopic dermatitis-like skin lesions, J. Ethnopharmacol. 295 (2022) 115428, https://doi.org/10.1016/j.jep.2022.115428.
[64] H.G. Li, Z. Zhang, H. Zhang, Y.F. Guo, Z.R. Yao, Update on the pathogenesis and therapy of atopic dermatitis, Clin. Rev. Allergy Immunol. 61 (3) (2021) 324–338, https://doi.org/10.1007/s12016-021-08880-3.
[65] L. Vinh, K.S. Lee, Y.K. Han, Y.J. Kim, S. Kim, A.B. Shah, Y. Byun, K.Y. Lee, Allergy inhibition using naturally occurring compounds targeting thymic stromal lymphopoietin pathways: a comprehensive review, Biomol. Ther. 33 (2) (2025) 249–267, https://doi.org/10.4062/biomolther.2024.177.
[66] C.C. Yue, H. Zhou, X.Y. Wang, J.D. Yu, Y.W. Hu, P. Zhou, et al., Atopic dermatitis: pathogenesis and therapeutic intervention, MedComm 5 (12) (2024) 70029, https://doi.org/10.1002/mco2.70029.
[67] M. Furue, T. Chiba, G. Tsuji, D. Ulzii, M. Kido-Nakahara, T. Nakahara, et al., Atopic dermatitis: immune deviation, barrier dysfunction, IgE autoreactivity and new therapies, Allergol. Int. 66 (3) (2017) 398–403, https://doi.org/10.1016/j.alit.2016.12.002.
[68] M. Bernard, C. Carrasco, L. Laoubi, B. Guiraud, A. Rozières, C. Goujon, et al., IL-1β induces thymic stromal lymphopoietin and an atopic dermatitis-like phenotype in reconstructed healthy human epidermis, J. Pathol. 242 (2) (2017) 234–245, https://doi.org/10.1002/path.4887.
[69] W.Y. Jin, W. Huang, L.Q. Chen, M.J. Jin, Q.M. Wang, Z.G. Gao, et al., Topical application of JAK1/JAK2 inhibitor momelotinib exhibits significant anti-inflammatory responses in DNCB-induced atopic dermatitis model mice, Int. J. Mol. Sci. 19 (12) (2018) 3973, https://doi.org/10.3390/ijms19123973.
[70] A. Tsiogka, M. Kyriazopoulou, G. Kontochristopoulos, E. Nicolaidou, A. Stratigos, D. Rigopoulos, et al., The JAK/STAT pathway and its selective inhibition in the treatment of atopic dermatitis: a systematic review, J. Clin. Med. 11 (15) (2022) 4431, https://doi.org/10.3390/jcm11154431.
[71] Z.X. Huang, X.J. Zhang, J. Li, L.J. Zhang, Y.H. Shen, R.R. Wang, et al., N-heterocyclic functionalized chalcone derivatives as anti-inflammatory agents for atopic dermatitis treatment by inhibiting JAK1/STAT3 signaling pathway, Bioorg. Chem. 156 (2025) 108200, https://doi.org/10.1016/j.bioorg.2025.108200.
[72] D.R. Menon, Y. Li, T. Yamauchi, D.G. Osborne, P.K. Vaddi, M.F. Wempe, Z.L. Zhai, et al., EGCG inhibits tumor growth in melanoma by targeting JAK-STAT signaling and its downstream PD-L1/PD-L2-PD1 axis in tumors and enhancing cytotoxic T-cell responses, Pharmaceuticals 14 (11) (2021) 1081, https://doi.org/10.3390/ph14111081.
[73] H. Tsuboi, K. Kouda, H. Takeuchi, M. Takigawa, Y. Masamoto, M. Takeuchi, et al., 8-Hydroxydeoxyguanosine in urine as an index of oxidative damage to DNA in the evaluation of atopic dermatitis, Br. J. Dermatol. 138 (6) (1998) 1033–1035, https://doi.org/10.1046/j.1365-2133.1998.02273.x.
[74] J. Lohakul, A. Chaiprasongsuk, S. Jeayeng, M. Saelim, P. Muanjumpon, S. Thanachaiphiwat, et al., The protective effect of polyherbal formulation, harak formula, on UVA-induced photoaging of human dermal fibroblasts and mouse skin promoting Nrf2-regulated antioxidant defense, Front. Pharmacol. 12 (2021) 649820, https://doi.org/10.3389/fphar.2021.649820.
[75] W. Zhou, D. Zeng, S. Liu, Y. Huang, F. Lv, W. Zhou, Histone deacetylase 3 inhibition alleviates 2,4-dinitrochlorobenzene-in-duced atopic dermatitis via epigenetically upregulating Nrf2/HO-1 signaling pathway, Int. Immunopharmacol. 126 (2024) 111107, https://doi.org/10.1016/j.intimp.2023.111107.
[76] J. Shi, M. Zhang, L.B. Zhang, H.P. Deng, Epigallocatechin-3-gallate attenuates microcystin-LR-induced apoptosis in human umbilical vein endothelial cells through activation of the NRF2/HO-1 pathway, Environ. Pollut. 239 (2018) 466–472, https://doi.org/10.1016/j.envpol.2018.04.038.
[77] Y. Zhao, X.H. Liu, X.J. Fu, Z.Y. Mo, Y. Jiang, Y.L. Yan, Protective effects of epigallocatechin gallate against ischemia reperfusion injury in rat skeletal muscle via activating Nrf2/HO-1 signaling pathway, Life Sci. 239 (2019) 117014, https://doi.org/10.1016/j.lfs.2019.117014.
[78] S.W. Ryter, Heme oxgenase-1, a cardinal modulator of regulated cell death and inflammation, Cells 10 (3) (2021) 515, https://doi.org/10.3390/cells10030515.
[79] M.V. Medina, D. Sapochnik, M.G. Sola, O. Coso, Regulation of the expression of heme oxygenase-1:Signal transduction, gene promoter activation, and beyond, Antioxid. Redox Signal. 32 (14) (2020) 1033–1044, https://doi.org/10.1089/ars.2019.7991.
[80] D. Wei, C.K. Qu, N. Zhao, S.Y. Li, N. Pu, Z.M. Song, Y. Tao, The significance of precisely regulating heme oxygenase-1 expression: another avenue for treating age-related ocular disease? Ageing Res. Rev. 97 (2024) 102308 https://doi.org/10.1016/j.arr.2024.102308.
[81] L. Chen, O. Martinez, L. Overbergh, C. Mathieu, B.S. Prabhakar, L.S. Chan, Early up-regulation of Th2 cytokines and late surge of Th1 cytokines in an atopic dermatitis model, Clin. Exp. Immunol. 138 (3) (2004) 375–387, https://doi.org/10.1111/j.1365-2249.2004.02649.x.
[82] F.N.U. Nutan, A.J. Kanwar, D. Parsad, The effect of topically applied corticosteroids on interleukin 1β levels in patients with atopic dermatitis, J. Eur. Acad. Dermatol. Venereol. 26 (8) (2012) 1020–1022, https://doi.org/10.1111/j.1468-3083.2011.04133.x.
[83] S. Salman, V. Paulet, K. Hardonnière, S. Kerdine-Römer, The role of NRF2 transcription factor in inflammatory skin diseases, Biofactors 51 (2) (2025) e70013, https://doi.org/10.1002/biof.70013.
[84] M. Koch, T. Kockmann, E. Rodriguez, U. Wehkamp, P. Hiebert, M.B. Greenwald, et al., Quantitative proteomics identifies reduced NRF2 activity and mitochondrial dysfunction in atopic dermatitis, J. Invest. Dermatol. 143 (2) (2023) 220–231, https://doi.org/10.1016/j.jid.2022.08.048.

[85] R. Ma, Y. Chang, Q.M.X. Chen, J.F. Li, B. Qiao, Precise PBAEs: a highly efficient single-molecularly defined gene-delivery system, Angew. Chem.-Int. Edit. 64 (19) (2025), https://doi.org/10.1002/anie.202422134.
[86] R.T. Oliynyk, G.M. Church, Circular vectors as an efficient, fully synthetic, cell-free approach for preparing small circular DNA as a plasmid substitute for guide RNA expression in CRISPR-Cas9 genome editing, Nat. Protoc. (2025), https://doi.org/10.1038/s41596-024-01138-0.
[87] K. Huang, D. Zapata, Y. Tang, Y. Teng, Y.M. Li, In vivo delivery of CRISPR-Cas9 genome editing components for therapeutic applications, Biomaterials 291 (2022) 121876, https://doi.org/10.1016/j.biomaterials.2022.121876.